REVIEW

Check for updates

Perylene diimide-based photocatalysts: from molecular design to emerging applications

Yin Xiao,[a] Zihe Chen,[a] Xin Liu,[a] Xusheng Wang, [ID][b] Guixiang Ding,[a] Zhaoqiang Wang,[a] Peng Wang*[c] and Guangfu Liao [ID] *[a]

Perylene diimide (PDI)-based semiconductor materials show significant promise for photocatalytic environmental decontamination and the conversion of energy resources but suffer from inefficient photocarrier separation which greatly limits their activity. Consequently, designing PDI-based photocatalysts to enhance carrier separation has become a major research focus. This persistent challenge has positioned the rational design of PDI-based architectures to enhance carrier dissociation kinetics and elevate functional efficacy as a central focus point of research in the field of contemporary photocatalysis. This review firstly examines recent progress in the rational design of PDI-based photocatalysts and their charge transfer mechanism. Then, advances in the fabrication of PDI photocatalysts and associated electron/hole transfer mechanisms are discussed. It systematically evaluates their enhanced activity in key applications: water splitting, CO_2 reduction, N_2 fixation, and pollutant degradation *etc.* Subsequently, the fundamental photocatalytic mechanism inherent to PDI-based materials is scrutinized in depth. Finally, outstanding issues and prospective uses for PDI-based photocatalysts are also discussed. It is believed that this review provides a valuable direction for engineering advanced PDI-based photocatalytic systems.

Wider impact

Conventional energy production exacerbates global environmental degradation, including climate change and greenhouse effects. Consequently, implementing sustainable renewable energy systems is imperative to mitigating impending energy crises, preserving ecological integrity, and achieving zero-emission targets with solar-driven artificial photosynthesis on advanced semiconductors representing a critical pathway for circular energy cycles. PDI semiconductor photocatalysts are prized for their economic viability, operational stability, superior photochemical responses, and electron-accepting capacity. This review systematically chronicles the evolution of PDI-based photocatalytic systems, combined with contemporary synthesis paradigms with emphasis on structural/functional modifications to advance semiconductor photocatalysis for solar energy harvesting. We further delineate persistent research challenges and strategic future directions. The transformative potential of these advanced materials underscores the imperative for cross-disciplinary convergence between materials chemistry and process engineering. Such synergies will catalyze innovative breakthroughs in semiconductor photocatalysis, accelerating the development of sustainable energy technologies. By consolidating design principles, mechanistic insights, and application landscapes, this work provides a foundational framework for researchers engaged in photocatalytic energy conversion and serves as a blueprint for engineering PDI photocatalysts.

1. Introduction

Global economic and industrial expansion exacerbates two critical challenges: environmental pollution and energy scarcity.[1–8] Semiconductor photocatalysis emerges as a promising

[a] College of Materials Engineering, Fujian Agriculture and Forestry University, Fuzhou 350002, China. E-mail: liaogf@mail2.sysu.edu.cn

[b] State Key Laboratory of Bio-based Fiber Materials, School of Materials Science and Engineering, Zhejiang Sci-Tech University, Hangzhou 310018, China

[c] CenerTech Tianjin Chemical Research & Design Institute Company, Ltd, Tianjin 300131, China. E-mail: lzuwangpeng@163.com

technology, efficiently enabling solar-to-chemical energy transformation through photoredox reactions for pollutant degradation,[9–11] CO_2 reduction,[12,13] and H_2 production.[14,15] This positions it as a key solution for environmental remediation and renewable energy. However, current limitations including short charge carrier lifetimes, insufficient sunlight utilization, poor stability, and low efficiency[16] hinder its practical deployment. Recently, organic semiconductor photocatalysts have proliferated due to their molecularly adjustable optoelectronic characteristics, structural versatility and cost-effective synthesis, *etc.*, with representative examples including covalent organic frameworks (COFs),[17] metal–organic frameworks (MOFs),[18] organic

polymers[19] and organic supramolecular compounds,[20] *etc.* Supramolecular organic semiconductors now constitute a rapidly developing photocatalytic domain, benefiting from precise synthetic control and broad spectral absorption capabilities. Among the organic semiconductors, PDI has garnered significant scientific attention due to its synthetic accessibility, cost-efficiency, and sustained functional integrity under photocatalytic conditions. Nevertheless, their photocatalytic performances remain hampered by inefficient charge separation kinetics and limited operational persistence.[21] Dating back to 1913, PDI first served as industrial dyes exhibiting robust durability, chemical resistance, thermal stability, lightfastness, and weatherability. The compound further reveals significant electronic properties beyond pigmentation, including substantial luminescence efficiency, excellent photo-stabilization capacity, and strong electron-accepting capability. Nowadays, PDI demonstrates significant applicability across multiple domains including sensors,[22] fluorescent switches,[23] fluorescent probes,[24] photoconductive materials,[25,26] and organic light-emitting diodes (OLEDs),[27] *etc.* A landmark 1997 study by Robert *et al.*[28] identified molecular PDI as a photocatalytic photosensitizer. Through photoinitiated energy transfer mechanisms, it produces singlet oxygen that mineralizes phenolic contaminants (*e.g.*, phenol) within controlled pH regimes.

Relative to molecular PDI, supramolecular constructs demonstrate advanced photocatalytic behavior, reflecting notable recent advancements in organic photocatalyst design.[29–33] Consequently, this has elevated research focus on PDI-based photocatalysts, centering on photogenerated charge behavior, molecular structure–function relationships, and oxidative/reductive reaction mechanisms. Non-covalent interactions – hydrogen bonding, dipole–dipole, π–π stacking, van der Waals, hydrophobic, and electrostatic forces – govern PDI supramolecular assembly. These approaches permit efficient organic photocatalytic architectures through mild, adaptable synthesis, outperforming covalent organic frameworks (COFs) in structural precision and synthetic economy while circumventing elaborate polymerization pathways.

This review analyzes recent progress in PDI-based photocatalytic architectures. Firstly, we introduce the molecular structure of PDI. Secondly, PDI-based photocatalysts are briefly summarized, including modifying the molecular engineering of PDI monomers (such as the substituents of side-chain and bay position), design of PDI polymers, heterojunction engineering (type-II, type-Z and type-S systems), metal deposition/doping, and construction of π–π composite systems, *etc.* Thirdly, the application of PDI-based photocatalysts including water splitting, CO_2 reduction, N_2 fixation, and pollutant degradation are summarized. Finally, the analysis concludes by outlining persistent challenges and forward-looking strategies for advanced photocatalyst design. This work aims to establish actionable frameworks for developing high-efficiency PDI materials that enable sustainable energy generation and environmental remediation.

Yin Xiao is currently pursuing her ME at the School of College of Material Engineering, Fujian Agriculture and Forestry University. Her research interests focus on photocatalysis, including the research of PDI monomer supramolecular materials.

Yin Xiao

Peng Wang received his PhD degree in physical chemistry from East China Normal University in 2018. Then he worked as a post-doc in Shanghai institute of Organic Chemistry (SIOC) and Leibniz Institute for Catalysis (LIKAT). He is currently a R&D Engineer. His research interests focus on the homogeneous catalysis and polymer synthesis & applications.

Peng Wang

Guangfu Liao received his PhD degree from Sun Yat-sen University in 2020. Then he was a Research Associate in The Chinese University of Hong Kong. Subsequently, he was a researcher at the China University of Geosciences. Now, he is a professor at Fujian Agriculture and Forestry University. His research interests involve photo & electrocatalysis, biomass energy, polymer synthesis & applications, etc. To date, he has published more than 80 high profile SCI papers such as in Nature Communications, Matter, Energy & Environmental Science, Angewandte Chemie International Edition, Advanced Functional Materials, etc. The awards he has received include the Youth Talent Promotion Project of the China Association for Science and Technology, Distinguished Professor of the "Minjiang Scholars" in Fujian Province, etc.

Guangfu Liao

2. Molecular structure of PDI

PDI is a derivative of polycyclic aromatic hydrocarbons,[34,35] featuring a perylene core symmetrically functionalized with dual imide groups (–CONHCO–)[36] Conventionally synthesized *via* terminal amidation of 3,4,9,10-perylenetetracarboxylic dianhydride (PTCDA) (Fig. 1a and b), its primary modification sites comprise terminal 'imide positions' and peripheral 'bay positions' (carbons 1, 6, 7, 12). Usually, the electron density at the nodes of the highest occupied molecular orbital (HOMO) and lowest unoccupied molecular orbital (LUMO) of PDI molecules nearly approaches zero, meaning that side-chain motifs do not readily engage in Π-electron conjugation with a perylene ring and fail to significantly affect the overall electronic structures of PDI molecules. Frontier molecular orbital analysis (Fig. 1c) reveals carbon and oxygen dominate HOMO/LUMO composition, while amide nitrogen exhibits negligible orbital contribution.[37] Modifications at the bay position alter the intrinsic energy levels and redox potential of PDI molecules, whereas substitutions at the imide position preserve these fundamental electronic properties and, consequently, their spectral absorption and emission characteristics. This methodology enables strategic modulation of imide substituents to probe structure–photoactivity relationships while conserving intrinsic orbital energetics.

The perylene ring of PDI features a rigid polycyclic π-conjugated framework, driving supramolecular assembly *via* π-orbital interactions. Typical interplanar distances in these stacked architectures measure 3.4–3.5 Å (Fig. 1d), mirroring
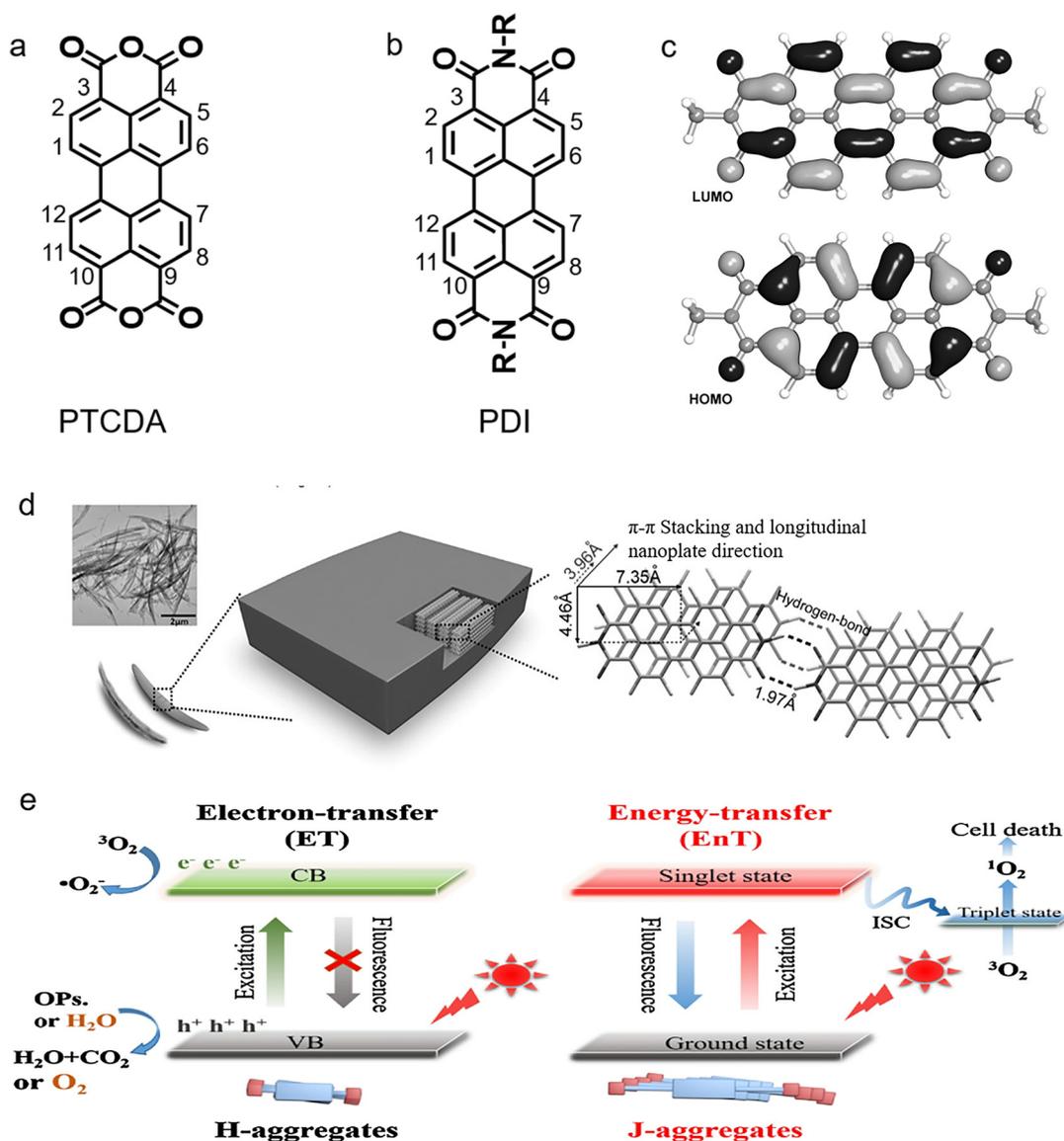

Fig. 1 (a) Molecular structures of PTCDA and (b) PDI which show the numbering of the positions in the ring system. (c) DFT calculations of frontier orbitals of *N,N'*-dimethyl PDI. Reproduced from ref. 37. Copyright 2011, American Chemical Society. (d) Size of a single PDINH molecule and the π–π stacking distance. Reproduced from ref. 38. Copyright 2016, Wiley. (e) H/J-aggregated PDI photocatalyst diagram representing the effect of (ET) and (EnT). Reproduced from ref. 41. Copyright 2018, Elsevier.

graphene's interlayer spacing.[38] Computational studies by Zhu *et al.* employing density functional theory (DFT) reveal enhanced π-stacking reduces PDI's band gap and lowers both HOMO/LUMO energy levels. Unlike monomers, supramolecular PDI exhibits semiconductor-like continuous bands due to non-covalent molecular ordering.[39] Würthner *et al.*[40] demonstrated that imide-position substituents modulate stacking configurations through steric and non-covalent effects. PDI aggregates primarily adopt H-aggregate or J-aggregate arrangements. H-aggregates display strong π-orbital overlap and extended conjugation, yielding semiconducting behavior. Conversely, J-aggregates maintain molecular photophysical properties due to reduced π-coupling. Mechanistic studies show H-aggregates facilitate electron transfer (ET): co-facial stacking creates π-delocalized channels enabling rapid electron migration to oxygen. J-aggregates favor energy transfer (EnT) processes. Upon photoexcitation, they efficiently generate triplet states *via* intersystem crossing, which enables them to act as potent photosensitizers (Fig. 1e). Spectroscopically, H-aggregates exhibit hypsochromically shifted absorption with fluorescence quenching and reduced quantum yields,[41] while J-aggregates exhibit bathochromic shifts without significant emission loss[42] making them the preferred fluorophores.[43] In photocatalysis, H-aggregates demonstrate superior potential due to deeper valence bands, enhanced charge mobility/separation, and stronger oxidative capacity.[44] This performance stems from PDI's planar aromatic structure mediating robust intermolecular π–π interactions.

3. Modification of PDI-based photocatalysts

Despite emerging as promising photocatalysts, nevertheless, the photocatalytic performance of PDI supramolecular systems is fundamentally constrained by three principal factors: elevated photogenerated exciton recombination rates, diminished charge transport kinetics, and insufficient oxidative capacity originating from low-lying VB positions.[45] Fundamentally, photocatalytic mechanisms comprise three consecutive processes: (i) photoexcitation across the semiconductor bandgap, (ii) spatial separation and transport of photogenerated charge carriers, and (iii) surface redox reactions. Consequently, rational material modifications primarily target two critical objectives: (i) broadening the spectral response range through bandgap engineering and/or sensitization strategies, and (ii) enhancing charge carrier dynamics by minimizing recombination losses while optimizing mobility pathways.[46] To overcome these inherent constraints, researchers have proposed many strategies including the design of PDI monomers and polymers, construction of π–π composite systems and heterojunctions system *etc.* This section provides a critical evaluation of contemporary advancements in enhancing the photocatalytic performance of PDI-based photocatalysts *via* these methods.

3.1. Monomer modification engineering

PDI, an n-type organic semiconductor and high-grade dye, features a polycyclic aromatic structure with an electron-rich perylene core and electron-withdrawing imide groups. This conjugation enables efficient charge carrier migration. PDI monomer architecture – determined by planar conjugation extent, substituent properties, and dipole moment – modulates intermolecular interactions (π–π stacking, electrostatic forces, hydrophobic effects, steric constraints). These interactions govern electronic wavefunction overlap and interchromophoric coupling, enabling precise engineering of supramolecular band structures. In this section, we primarily discuss the influence of substituent groups on the molecular properties of PDI monomers (Table 1 and Fig. 3). Substitution at the imide (*N*-substitution) and bay positions of PDI molecules serves as a fundamental strategy for precisely tuning their photophysical properties, molecular stacking behavior, and photocatalytic performance.

3.1.1. Side-chain substituents. The imide side-chain substituents of molecular PDI serve as critical structural determinants that govern solubility characteristics, supramolecular organization, and consequently, photocatalytic performance metrics. Through deliberate side-chain functionalization, precise modulation of intermolecular packing geometries, charge carrier dynamics, and optoelectronic properties can be achieved. Synthetically, PDIs are typically prepared *via* condensation of 3,4,9,10-perylenetetracarboxylic dianhydride (PTCDA) with functional groups (alkyl, amino, carboxyl, or aromatic moieties), under an inert atmosphere, employing solvents such as tetrahydrofuran, imidazole, or quinoline, *etc.*, as the solvent, which primarily regulates intermolecular interactions and solubility. This section presents a comprehensive analysis of side-chain classification, systematically evaluating their respective merits and limitations, while elucidating their profound influence on fundamental photocatalytic parameters including electronic band structure, charge transport efficiency, and interfacial charge transfer kinetics.

Alkyl chains, as one of the most prevalent imide side-chain modifications in PDI systems, demonstrate substantial influence on photocatalytic performance through three primary mechanisms: solubility modulation, molecular packing control, and charge transfer regulation. From a solubility perspective, the introduction of alkyl chains effectively attenuates the strong intermolecular π–π interactions characteristic of PDI derivatives. This attenuation effect not only prevents excessive molecular aggregation but also significantly enhances solubility in organic solvents including chloroform and toluene.[47–50] The resultant increase in accessible catalytically active sites substantially improves interfacial contact between the photocatalyst and organic substrates. However, the inherent nonpolar nature of alkyl chains presents limitations in polar reaction media.[51] Specifically, their weak interactions with aqueous phases and metal oxide surfaces create substantial barriers for efficient charge transfer processes in aqueous photocatalytic systems, as evidenced by reduced quantum yields in water-splitting applications. Regarding molecular organization, alkyl chains – particularly those with optimized length (C6–C12) and branching patterns – induce a distinctive J-type stacking configuration through steric repulsion effects. This packing mode exhibits two critical characteristics: (1) it generates a moderately widened

Table 1 Summary of the photocatalytic activity of PDI monomer photocatalysts

Photocatalysts	The amount of catalyst (mg)	Morphology	Source of light	Photocatalytic application	Performance	AQY	Ref.
1	25	Nanosheets	Xenon lamp, 300 W, $\lambda > 420$ nm	Pollutant Phenol Catechol BPA 4-CP	 1.23 (h^{-1}) 1.46 (h^{-1}) 2.77 (h^{-1}) 2.08 (h^{-1})	—	68
4	25	Nanobelts	White LED, 5 W	Pollutant TC MB RhB	 0.71 (h^{-1}) 1.24 (h^{-1}) 0.55 (h^{-1})	—	57
5	25	Ultrathin nanosheets	Xenon lamp, 500 W, $\lambda > 420$ nm	Pollutant Phenol OTC EE	 0.51 (h^{-1}) 0.65 (h^{-1}) 0.55 (h^{-1})		33
6	50	Nanobelts	Xenon lamp, 300 W, $\lambda > 420$ nm	H_2 production	11 700 (μmol h^{-1} g^{-1})	2.96 (550 nm)	62
7b	25	Nanosheets	Xenon lamp, 300/500 W, $\lambda > 420$ nm,	Pollutant phenol/O_2 production	1.45 (h^{-1})/2490 (μmol h^{-1} g^{-1})	—	69
8	25	2D layers with flaky	Xenon lamp, 1000 W, $\lambda > 420$ nm	Pollutant MB DCF	 0.262 (h^{-1}) 0.172 (h^{-1})	—	30
9c	25	Nanobelt	Xenon lamp, 500 W, $\lambda > 420$ nm	Pollutant phenol/O_2 production	3.96 (h^{-1})/11 700 (μmol h^{-1} g^{-1})	—	56
10	25	Nanofibers	Xenon lamp, 500 W, $\lambda > 420$ nm	Pollutant phenol	0.129 (h^{-1})	—	39
11	—	—	White LED array	H_2O_2 production	—	<1%	70

bandgap (2.2–2.5 eV) due to decreased orbital overlap, and (2) facilitates the formation of highly ordered one-dimensional nanostructures.[52] Spectroscopically, the J-aggregation induced by alkyl side chains produces a pronounced bathochromic shift in the absorption spectrum. This redshift effect extends the visible light harvesting range to longer wavelengths ($\lambda > 550$ nm),[53] thereby enhancing solar energy utilization efficiency in optimized systems. While the application of alkyl-modified PDIs in polar reaction environments remains challenging, their unparalleled ability to precisely control fundamental material properties makes them indispensable for photocatalytic applications involving nonpolar substrates. The structure–property relationships established in these systems provide valuable design principles for developing advanced organic photocatalysts. For instance, Wang et al.[41] synthesized PDI derivatives with different alkyl chain lengths (H-PDI and J-PDI) via a pH-triggered hydrogelation method, systematically investigating the influence of side-chain substituents on photocatalytic performance. The study revealed that H-PDI with shorter side chains formed face-to-face π–π stacking, known as H-aggregation, exhibiting semiconductor characteristics with a narrowed bandgap of 1.69 eV. This configuration predominantly facilitated electron transfer, generating superoxide radicals and holes, which demonstrated superior activity for phenol degradation under visible light with a rate constant of 0.195 h^{-1}. In contrast, J-PDI with longer side chains adopted a head-to-tail stacking mode, referred to as J-aggregation with a bandgap of 1.78 eV, which promoted energy transfer and efficiently produced singlet oxygen with a high quantum yield of 0.66. Under 600 nm red light irradiation, J-PDI exhibited significantly enhanced inhibition of HeLa cells compared to H-PDI. This work elucidates how side-chain engineering can precisely modulate supramolecular

packing to optimize photocatalytic pathways, providing a novel strategy for designing tailored photocatalysts for environmental remediation and antitumor applications.

Aromatic or rigid side chains, such as phenyl, naphthyl, or cycloalkyl groups (e.g., 4-tert-butylphenyl), exert a distinct influence on the photocatalytic performance of PDI molecules through their impact on molecular stacking, stability, and electronic interactions.[52] These rigid aromatic moieties strengthen intermolecular π–π stacking via additional aromatic interactions, which enhances charge delocalization across the PDI backbone and improves photostability by reducing structural fluctuations under light irradiation – an advantage for long-term catalytic reactions. However, their large steric volume and strong intermolecular interactions led to poor solubility in both organic solvents and aqueous media, limiting the processability of PDI and potentially causing excessive aggregation that reduces the accessible catalytic active sites.[54] In terms of molecular packing, aromatic side chains induce a face-to-face H-type stacking mode with a relatively small d-spacing (approximately 3.5 Å), which narrows the band gap of PDI, enabling stronger absorption of visible light. Nevertheless, the tight and rigid stacking increases carrier scattering, resulting in lower charge mobility compared to alkyl-modified PDI. This trade-off between strong light absorption and moderate charge mobility makes aromatic-modified PDI particularly suitable for photocatalytic reactions requiring high oxidizing power and selectivity. Overall, aromatic or rigid side chains play a unique role in optimizing PDI's performance in selective organic synthesis and reactions demanding high stability.[55] For example, Zhu et al.[56] implemented a σ-spacer length optimization strategy to augment charge mobility in imidazole-alkyl-perylene diimide (IMZ-alkyl-PDI) photocatalysts with donor–spacer–acceptor

(D–σ–A) architecture through precise π–π stacking distance regulation (Fig. 2a). Among the series – non-alkylated (C0IPDI), ethyl-bridged (C2IPDI), and propyl-modified (C3IPDI) – the ethyl linkage achieved minimal π–π separation (3.19 Å) by steric minimization between donor/acceptor units, elucidating intrinsic photocarrier transport mechanisms. C2IPDI demonstrated exceptional photocatalytic enhancement: 32-fold greater phenol degradation efficiency *versus* IMZ-PDI, alongside a 271-fold increase in oxygen evolution (Fig. 2b and c). Moreover, Sun and coworkers[33] engineered an ultrathin porous hp-PDI-NA photocatalyst *via* nicotinic acid terminal substitution (Fig. 2d). It demonstrated 3.5-fold higher visible-light phenol degradation activity than nano-PDI, achieving near-complete mineralization. The catalyst retained 98% activity after 5 cycles, and effectively mineralized antibiotics (oxytetracycline) and hormones (ethinylestradiol) (Fig. 2e). Combined characterization/theory revealed its enhanced performance stems from a bi-planar conformation and hierarchically porous nanosheet morphology. NA substitution reduces steric hindrance, strengthens π–π conjugation, and shortens interlayer spacing, thereby boosting carrier separation/transport and structural stability

(Fig. 2f). Although aromatic substituents further extend conjugation, narrowing the bandgap for enhanced visible-light absorption which offers critical advantages including improved processability for homogeneous composite formation, tunable stacking distances for efficient charge transport, and increased surface hydrophilicity to facilitate pollutant adsorption and water activation, bulky groups may disrupt π-conjugation and increase charge transport resistance, excessive intermolecular interactions can reduce active site accessibility, and chemically unstable substituents (*e.g.*, certain alkyl amines) may degrade under prolonged irradiation, compromising catalytic durability. To enhance photocatalytic performance, functional group modifications are employed.

Polar functionalized chains, such as those bearing carboxyl (–COOH)[39,57] or amine (–NH$_2$)[58] groups (*e.g.*, glycine or polyethylene glycol derivatives), play a crucial role in regulating the photocatalytic performance of PDI molecules through their influence on solubility, intermolecular interactions, and heterojunction formation. These polar groups significantly enhance the water solubility of PDI, addressing the issue of poor dispersibility in aqueous systems that limits the accessibility of catalytic active
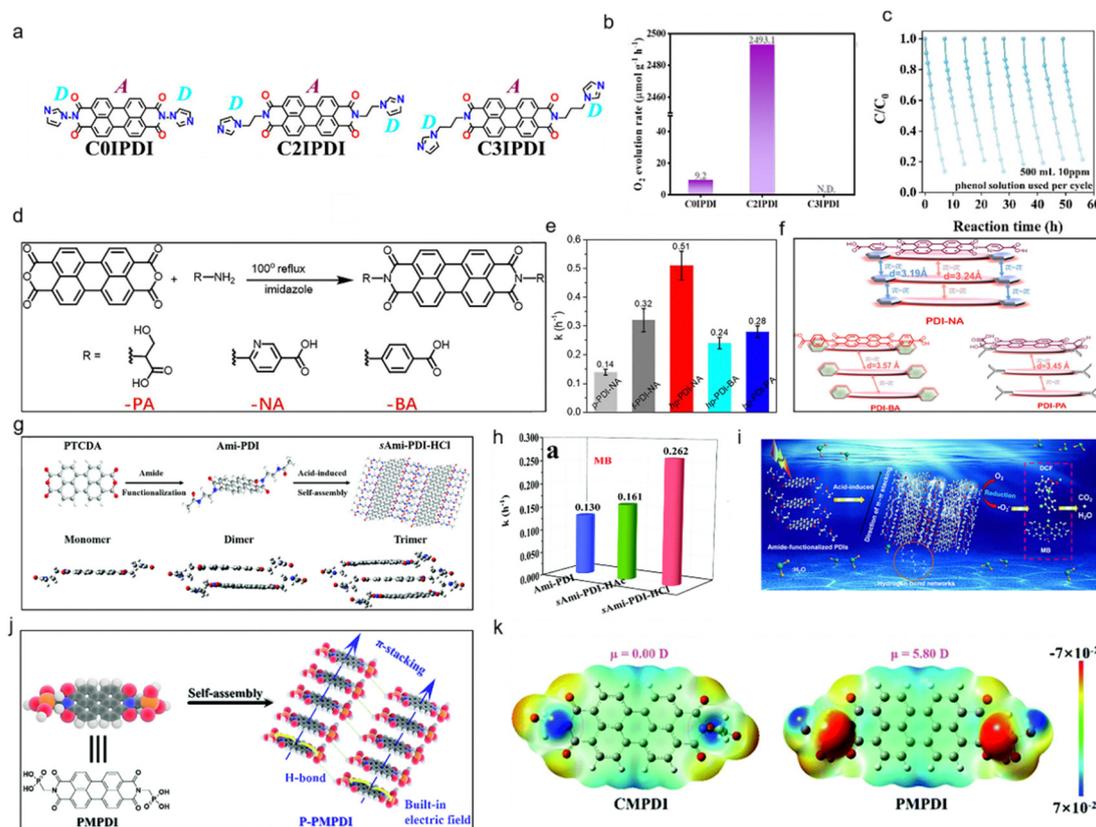

Fig. 2 (a) Different σ lengths of molecular structures about CnIPDI. (b) Comparison of photocatalytic O$_2$ evolution rate on CnIPDI. (c) Cyclic stability of C2IPDI. Reproduced from ref. 56. Copyright 2023, Wiley. (d) The synthesis method of PDI-NA molecular and reference catalyst. (e) TOC removal rate and mineralization rate constant over different photocatalysts. (f) A schematic diagram of PDI-NA, PDI-BA and PDI-PA. Reproduced from ref. 33. Copyright 2022, Elsevier. (g) The synthesis process and structure of sAmi-PDI-HCl (over) and the DFT calculations regarding geometries of sAmi-PDI-HCl monomers, dimers, and trimers (below). (h) The kinetics constants toward MB. (i) The mechanism for the photocatalytic degradation process when using amide-functionalized supramolecular PDI. Reproduced from ref. 30 Copyright 2020, the Royal Society of Chemistry. (j) The synthesis of supramolecular P-PMPDI. (k) Diagram of molecular dipoles and electron distribution in PDI derivatives. Reproduced from ref. 62. Copyright 2019, the Royal Society of Chemistry.

sites, thereby facilitating contact with water-soluble pollutants and improving reaction kinetics. Additionally, the polar nature of these side chains enables strong hydrogen bonding or electrostatic interactions with metal oxides (*e.g.*, TiO_2, $BiOCl$, *etc.*) or metal ions (*e.g.*, Zn^{2+}),[59] which is critical for the formation of stable heterojunctions; such heterojunctions promote efficient interfacial charge transfer, reducing the recombination rate of photogenerated electrons and holes. For instance, carboxyl-functionalized PDI can form a close heterojunction with $BiOCl$,[60] where the interfacial charge transfer is accelerated, significantly increasing the generation of hydroxyl radicals (•OH) and resulting in a threefold enhancement in phenol degradation efficiency compared to alkyl-modified PDI. However, these polar side chains can also induce excessive intermolecular interactions, leading to H-type aggregation in some cases, which may narrow the visible-light absorption range and increase electron–hole recombination, thereby partially offsetting the positive effects. In terms of molecular stacking, the polar interactions between these side chains tighten the π–π stacking, which narrows the band gap of PDI, allowing for better utilization of visible light. Overall, polar functionalized chains are particularly advantageous in aqueous photocatalytic systems and heterojunction-based catalytic systems, despite their potential to induce unfavorable aggregation, their ability to enhance solubility and promote charge transfer makes them indispensable in optimizing PDI's photocatalytic performance. For example, Li *et al.*[30] engineered an intralayer polarization field within amide-functionalized PDI supramolecular assemblies (sAmi-PDI) (Fig. 2g). π–π stacking and hydrogen bonding synergistically enhance polarization while constructing electron–hole transfer bridges and accelerating carrier separation. The acidic medium optimized electrostatic interactions and provided abundant electron donors/acceptors, boosting self-assembly efficiency. Benefitting from these effects, sAmi-PDI exhibited twofold-enhanced photocatalytic activity in pollutant degradation. The polarization field – originating from supramolecular networks – enables rapid carrier migration, establishing a green synthesis paradigm for high-performance PDI photocatalysts (Fig. 2h and i). Guo *et al.*[61] synthesized engineered an oxygen-deficient PDI supramolecular system (R-Ov-PDI) to optimize hole migration kinetics. Photoinduced holes were preferentially trapped at anionic defect centers, triggering an attack on the C–N bond. Remarkably, visible-light-driven benzylamine photooxidation achieved a benchmark efficiency of 31.3 mmol g^{-1} h^{-1} with >99% imine selectivity. Moreover, Kong *et al.*[62] engineered the preparation of a noncovalent self-assembled phosphoric acid-substituted PDI (PMPDI) (Fig. 2j). Functionalization with electron-withdrawing terminal groups (Fig. 2k) enhanced photocatalytic performance through improved exciton dissociation and extended photon harvesting range. Pu *et al.*[57] synthesized a series of asymmetrically structured PDI supramolecular photocatalysts (PDI-CH_3, PDI-NH_2, and PDI-COOH) *via* terminal group modification of imide positions, aiming to enhance the internal electric field (IEF) through molecular dipole engineering. Density functional theory (DFT) calculations revealed that the electron-withdrawing –COOH group in PDI-COOH induced the largest dipole moment (2.3257 D), followed by PDI-NH_2 (1.1715 D) and PDI-CH_3 (0.0034 D), directly correlating

with IEF intensity (PDI-COOH: 8.4 × PDI-CH_3). This enhanced IEF significantly improved charge separation efficiency from 4.6% (PDI-CH_3) to 11.2% (PDI-COOH), as confirmed by photoelectrochemical tests and surface photovoltage spectroscopy. The work demonstrates that asymmetric molecular design amplifies IEF to simultaneously boost oxidative and reductive photocatalytic activities, offering a universal strategy for organic photocatalyst optimization.

3.1.2. Bay sites substituents engineering. Functionalization of the bay sites in PDI molecules through electron-withdrawing or electron-donating groups represents a viable strategy for modulating both the electronic properties of individual PDI units and their subsequent supramolecular organization. As discussed in the referenced studies,[63] bay sites substituents are critical for tailoring photocatalytic performance through their modulation of molecular geometry, stacking modes (modification to perylene rings would affect PDI self-assembled arrangements since perylene rings are twisted more seriously due to the steric hindrance of substituents), and electronic properties, with distinct advantages and limitations associated with specific substituent types.[64,65] Halogens (*e.g.*, Cl)[66] and electron-withdrawing groups[67] are prominent examples: halogenation enhances intermolecular π–π stacking by reducing steric hindrance, leading to ordered one-dimensional packing with a *d*-spacing of ∼3.3–3.5 Å, which facilitates efficient charge delocalization and increases electron mobility, while cyano groups lower the LUMO energy level, promoting electron transfer to O_2 for the generation of reactive oxygen species (*e.g.*, •O_2^-) crucial for pollutant degradation.[67] However, excessive substitution can induce torsional angles in the perylene core, disrupting the planar π-conjugation and widening the band gap, thereby reducing visible-light absorption efficiency, and bulky substituents (*e.g.*, phenoxy groups) may weaken π–π interactions, resulting in loose stacking and increased carrier recombination.[65] These substituents directly govern stacking modes, which in turn dictate photocatalytic activity. For example, Zhang *et al.*[66] synthesized three PDI molecules with different bay substitutions: H_2PDI, 2Br–H_2PDI, and 4CH_3CH_2O–H_2PDI which formed 1D nanorods, 2D nanosheets, and 0D nanoparticles respectively. The bay substitutions altered the molecular geometry and stacking modes: H_2PDI had a planar structure with strong π–π stacking, 2Br–H_2PDI showed a twisted perylene core with weakened π–π interactions but enhanced hydrogen bonding; 4CH_3CH_2O–H_2PDI exhibited significant distortion due to steric hindrance, leading to loose stacking. These structural changes directly affected the photocatalytic performance: the narrower band gaps (1.62 eV and 1.68 eV) *vs.* 2.02 eV of H_2PDI, 2Br–H_2PDI, and 4CH_3CH_2O–H_2PDI improved charge separation and transfer efficiency, as evidenced by higher photocurrent density and lower electrochemical impedance. Consequently, they displayed superior photocatalytic activity, with 2Br–H_2PDI achieving 11-fold and 1.4-fold higher rates in the oxygen evolution reaction (OER) and generation of H_2O_2 than H_2PDI, while 4CH_3CH_2O–H_2PDI showed 20-fold and 4-fold enhancements, respectively. Notably they could efficiently produce H_2O_2 from
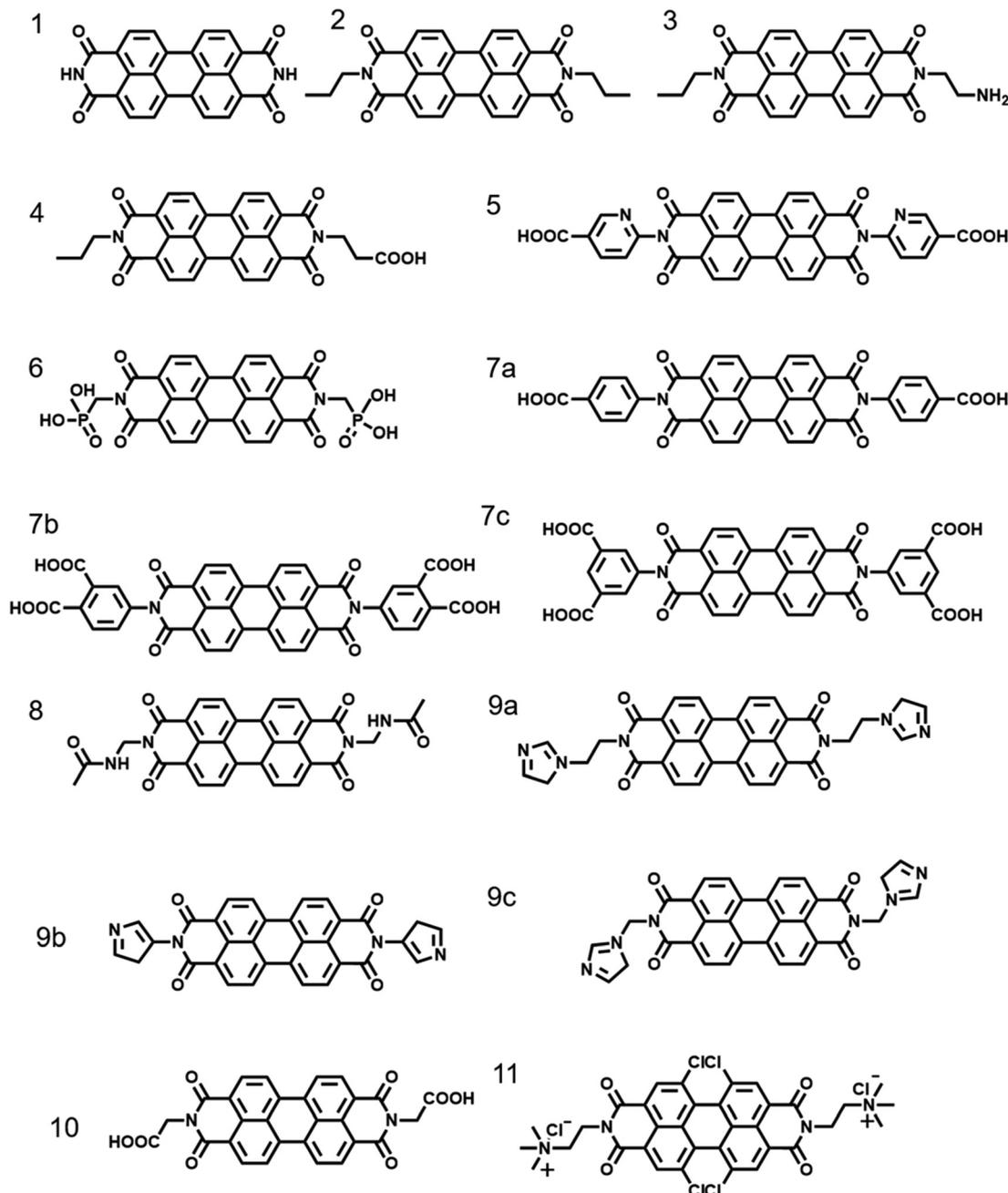
Fig. 3 Structures of PDI photocatalysts modified by imide-positions and bay-positions.

O_2 and H_2O without sacrificial agents, demonstrating the critical role of bay substitution in regulating PDI's photocatalytic performance through structural modulation.

3.2. Polymer modification engineering

The limited stability of PDI supramolecular materials, stemming from weak non-covalent interactions, presents a significant challenge. Replacing these interactions with directional covalent linkages between PDI monomers would simultaneously enhance structural integrity and preserve the uninterrupted π-delocalization channels essential for rapid electron migration. Zhang's group[71] fabricated crystalline urea-PDI materials,

achieving an oxygen evolution rate of 3223.9 μmol μmol g^{-1} h^{-1} with an apparent quantum yield (AQY) of 3.86% at 450 nm illumination (Fig. 4a and b). The combined effect of crystallinity and molecular dipole moment established a potent IEF. This configuration facilitated effective charge separation and sustains photocatalytic activity for over 100 hours (Fig. 4c). Subsequently, in Cao's work[72] 1D Co-UPDI nanocrystals were synthesized *via* Co^{2+}-UPDI assembly, achieving a record POE rate in $AgNO_3$ colloids, which was 10 times higher than that of UPDI alone. Co–N coordination enhances H-stacking rigidity and enabled *in situ* CoOOH formation. Wu *et al.*[73] prepared non-continuous conjugated semiconductor EDA-PTCDA nanosheets using an uncomplicated
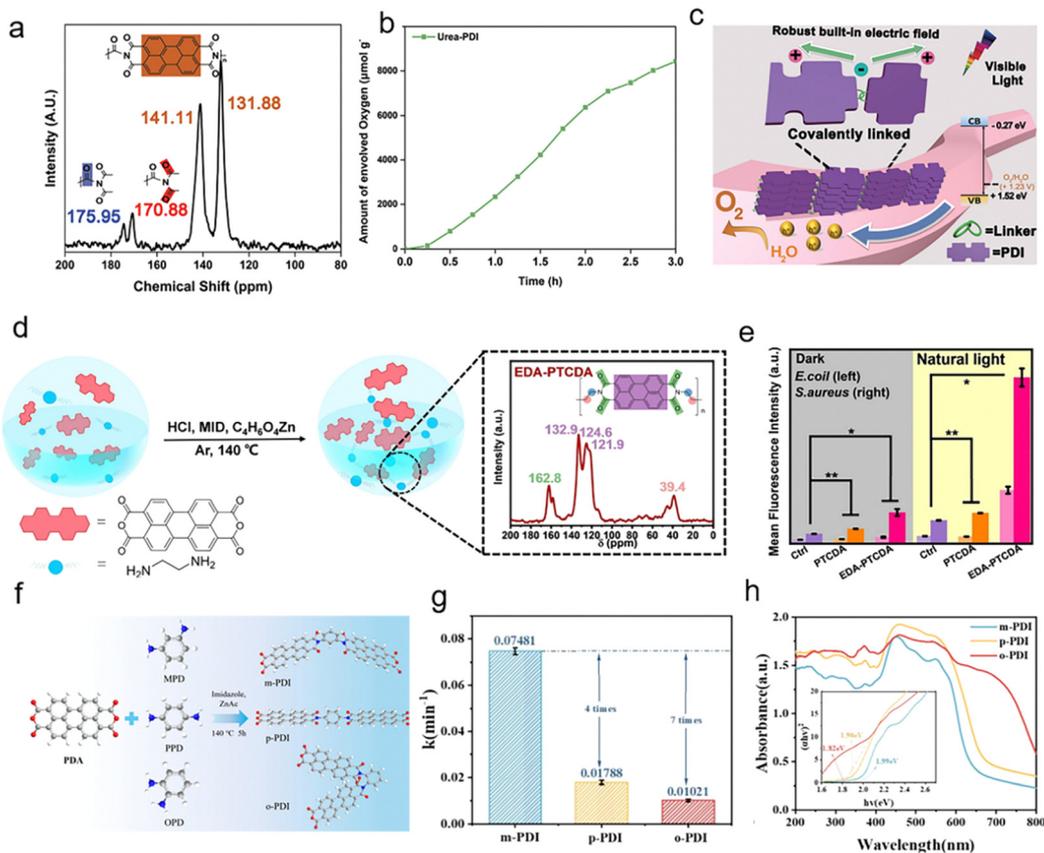
Fig. 4 (a) Solid ^{13}C NMR spectrum of urea-PDI. (b) The photocatalytic oxygen evolution with urea-PDI. (c) Mechanism diagram of the urea-PDI polymer photocatalyst. Reproduced from ref. 71. Copyright 2020, Wiley. (d) EDA-PTCDA synthetic methods and solid state ^{13}C NMR spectrum. (e) Quantitative analysis of intracellular ROS before and after natural light irradiation. Reproduced from ref. 73. Copyright 2023, Wiley. (f) Diagram of photocatalyst synthesis. (g) Comparison of degradation rate constants of three materials. (h) UV-vis absorption spectra of *m*-PDI, *p*-PDI and *o*-PDI. Reproduced from ref. 75. Copyright 2024, Elsevier.

solvothermal approach assisted by acidification (Fig. 4d). Significant molecular dipole anisotropy enabled efficient partitioning and trapping of photogenerated electron–hole pairs. This polymer demonstrates stable, continuous reactive oxygen species (ROS) production under natural sunlight, conferring effective microbicidal action against both Gram-positive and Gram-negative bacterial strains (Fig. 4e). Huang's[74] group synthesized a 3D porous PDI-CTS polymer photocatalyst with a donor–acceptor (D–A) structure. It exhibited a remarkable bisphenol A degradation rate (0.343 min^{-1}) through persulfate radical generation. Donor–acceptor synergy accelerated interfacial charge migration, creating a larger dipole moment and a 6.9-fold stronger IEF than pure PDCTA, greatly facilitating photogenerated carrier separation. Recently, Huang *et al.*[75] synthesized *m*-, *p*-, and *o*-PDI polymers by coupling PDI with benzene diamines at distinct positions to enhance charge carrier separation (Fig. 4f). Distinct linkage configurations modulated specific surface area, band energetics, and charge transport behavior. Among these, *m*-PDI demonstrated maximal interfacial exposure and the most negative VB position, while its distinctive architecture enhanced ofloxacin (OFL) adsorption affinity and electron transfer kinetics. Consequently, *m*-PDI achieved a 0.07481 min^{-1} OFL degradation rate (60 min, light) with robust stability in aquatic environments

(Fig. 4g and h). Recent representative studies (Fig. 5 and Table 2) highlight three principal merits of (PDI)-based polymers: (1) inherent high crystallinity substantially improves charge transport efficiency; (2) significant molecular dipoles facilitate formation of intensified IEF, enabling accelerated movement of photoinduced charges; (3) relative to supramolecular PDI systems, covalently bonded architectures demonstrate enhanced structural integrity.

3.3. Heterojunction engineering

While a narrow bandgap enhances solar energy utilization in photocatalysts, it concomitantly promotes photoinduced charge recombination. Conversely, wide bandgaps suppress recombination and preserve strong redox potentials for charge carriers, yet excessively wide gaps limit broad-spectrum photon harvesting. To resolve this trade-off – termed the 'single-component bottleneck' – heterojunction engineering provides an effective strategy. Heterojunction photocatalysts comprise two or more distinct semiconductor components, establishing an IEF at their material interfaces. This IEF serves as the primary impetus for photogenerated charge transfer, effectively prolonging carrier lifetimes while minimizing recombination rates.[79–81] This approach increases the lifetime of photo-generated charges and reduces
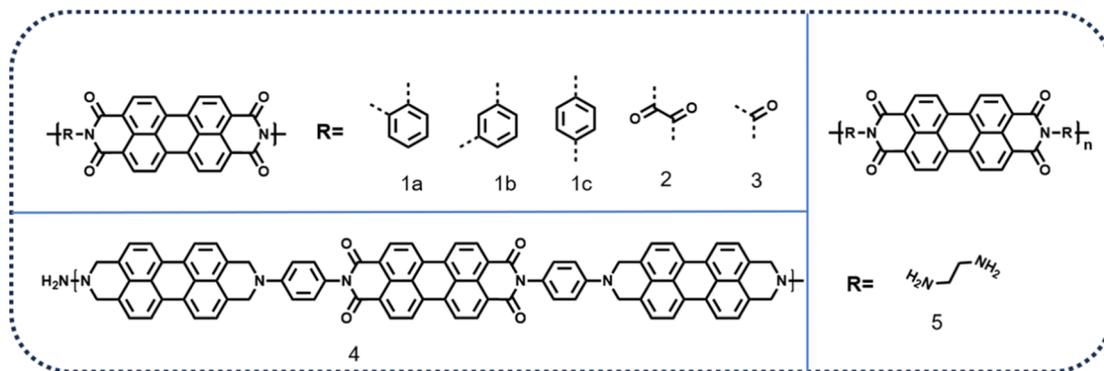
Fig. 5   Structure of PDI polymer photocatalysts.

Table 2   Summary of the photocatalytic activity of PDI polymer typical photocatalysts

Photocatalysts	The amount of catalyst	Morphology	Source of light	Photocatalytic application	Performance	AQY	Ref.
1a	—	Uniform nanosheet	AM1.5G	Water splitting	Photocurrent density 115.1 (μA cm^{-2})	—	76
2	25	Ultrathin sheets	Xenon lamp, 300 W	O$_2$	5110.25 (μmol h^{-1} g^{-1})	2.15 (420 nm)	77
3	25	Nanobelt	Xenon lamp, 300 W, $\lambda > 420$ nm	O$_2$	3223.9 (μmol h^{-1} g^{-1})	3.86 (450 nm)	71
4	10	Layer structure	LED lamp, 100 W	Pollutant Cr	2.04 (h^{-1})	—	78
5		Nanosheets	Natural light source	Antibacterial *Escherichia coli/Staphylococcus aureus*	within 60/45 min	—	73

their recombination. In addition, the construction of a heterojunction can also optimize the band positions and facilitate surface catalytic reactions. Contemporary advances in PDI-based heterojunctions utilize these principles to boost photocatalytic efficiency for solar fuel production and pollutant degradation. These systems are categorized primarily by charge transfer mechanism into three classes: type-II, Z-scheme, and S-scheme heterojunctions incorporating PDI. The subsequent portion methodically reviews seminal recent developments in PDI-based heterostructure photocatalysts.

3.3.1. PDI-based type-II heterojunctions. As shown in Fig. 6, type-II heterojunctions possess a staggered gap. Semiconductor A exhibits higher conduction band (CB) and valence band (VB) energies relative to those of semiconductor B. Following photon absorption, thermodynamic gradients propel electrons

toward semiconductor B's CB and holes toward semiconductor A's VB. This charge redistribution establishes an IEF, which further promotes directional segregation of charge carriers. Therefore, electrons accumulate in semiconductor B while holes localize in semiconductor A, significantly enhancing photocatalytic activity. Significantly, when excitation occurs exclusively in one semiconductor component, its counterpart functions solely as charge reservoirs. Consequently, type-II heterojunctions achieve enhanced carrier separation at the expense of compromised oxidation/reduction capabilities. This review examines advancements in PDI-based type-II heterostructure composites.

Bismuth-based photocatalysts have emerged as prominent materials due to their extended light-harvesting range, modifiable energy band characteristics, and unique electronic properties. However, persistent limitations include inadequate photon capture efficiency and structural instability. A promising strategy to mitigate these constraints involves constructing heterostructures through integration of PDIs with these photocatalytic systems. For instance, Zhang *et al.*[82] synthesized Bi$_2$WO$_6$/PDI heterojunctions *via* water bath heating. Under visible light, the Bi$_2$WO$_6$/PDI heterojunction exhibited higher phenol degradation rates than pure Bi$_2$WO$_6$ or self-assembled PDI, and doubled the oxygen production rate of pure PDI (Fig. 7b and c). The enhanced activity stems from the formation of an n–n type-II heterojunction which has a staggered band alignment facilitating charge separation (Fig. 7a).

Research in photocatalysis indicates the considerable potential of nonmetallic carbon-based semiconductors due to their superior optoelectronic characteristics and eco-compatibility. Type-II heterojunctions between PDIs and carbon materials have also gained increasing attention for applications. Particularly
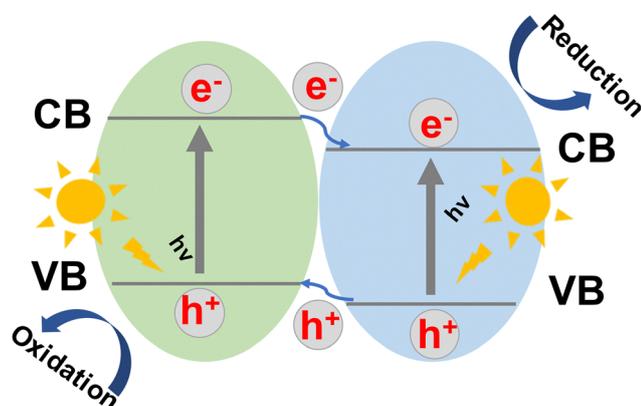

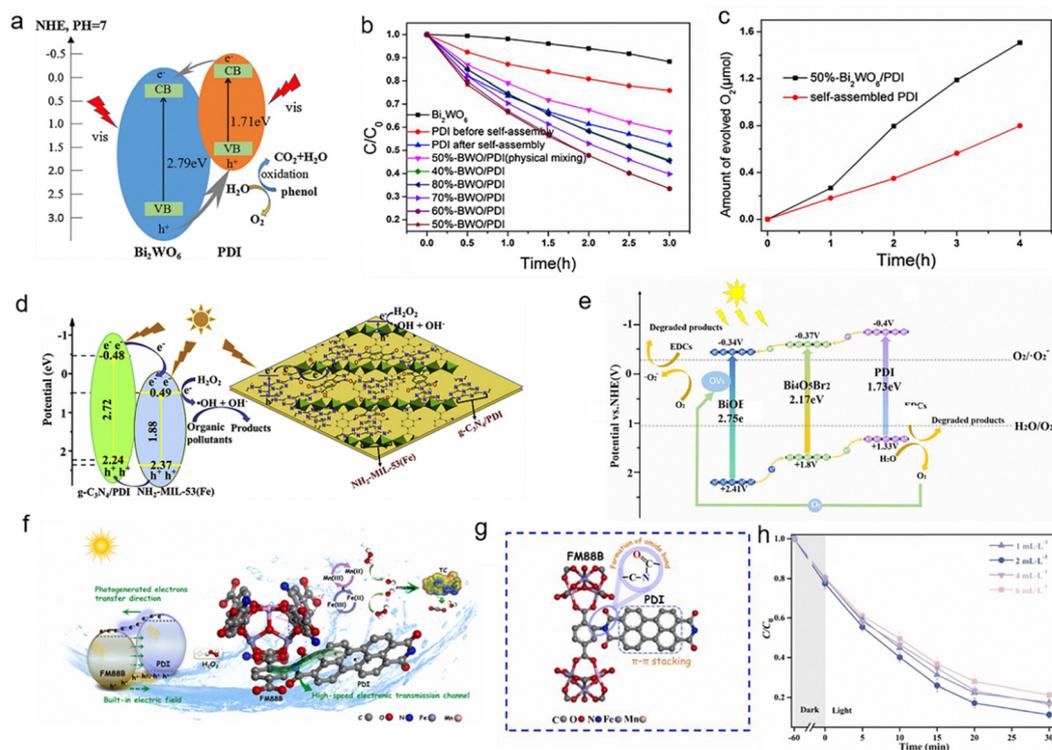Fig. 6   Charge transfer mechanism in type-II heterojunctions.

Fig. 7 (a) The possible reaction mechanism of Bi_2WO_6/PDI composite materials. (b) Photocatalytic degradation of 5 ppm phenol. (c) Oxygen evolution from water by PDI and the 50%–Bi_2WO_6/PDI sample in the presence of an electron acceptor. Reproduced from ref. 82 Copyright 2018, Elsevier. (d) The possible photocatalytic mechanism of the CPM-2 composite under visible light irradiation. Reproduced from ref. 83. Copyright 2019, Elsevier. (e) Possible photocatalytic mechanism of the BiOBr/$Bi_4O_5Br_2$/PDI system. Reproduced from ref. 84. Copyright 2022, Elsevier. (f) Degradation mechanism of TC in the system of visible light/6%PDI/FM88B/H_2O_2. (g) Ammoniation reaction between PDI and FM88B. (h) Effect of H_2O_2 concentration on the degradation efficiency of TC over 6%PDI/FM88B. Reproduced from ref. 85. Copyright 2024, Elsevier.

noteworthy are n-type graphitic carbon nitride (g-C_3N_4) photocatalysts, which represent the most extensively investigated system in this category. Li *et al.*[83] synthesized a g-C_3N_4/PDI@NH_2-MIL-53(Fe) (CPM) type-II heterojunction *via* thermal polymerization, surface growth, and solvothermal methods (Fig. 7d). The CPM heterojunction demonstrated exceptional visible-light photocatalytic activity with H_2O_2, degrading aqueous pollutants rapidly. This superior performance stems from the optimized type-II heterojunction. Close interfacial contact and aligned band structures between g-C_3N_4/PDI and NH_2-MIL-53(Fe) enhance charge separation.

Ternary or multicomponent systems enhance carrier separation efficiency through synergistic effects. Wang *et al.*[84] developed a visible-light-responsive BiOBr/$Bi_4O_5Br_2$/PDI dual heterojunction photocatalyst for efficient degradation of endocrine-disrupting chemicals (EDCs) in water (Fig. 7e). The aligned energy bands between $Bi_4O_5Br_2$ and BiOBr promote heterojunction formation, improving space-charge separation. Simultaneously, PDI loading extends the photo-response range while facilitating carrier transfer and separation. Within this dual-heterojunction system: (1) electrons migrate to BiOBr's CB. (2) Holes accumulate on PDI's VB. This charge separation enables H_2O oxidation to O_2 followed by $\cdot O_2^-$ formation through reduction. Notably, photocatalytic activity persists significantly under anoxic conditions.

Metal–organic frameworks (MOFs) constitute porosity-defined crystalline solids formed by metal nodes cross-linked to organic

molecular bridges. Their extensive surface exposure, abundant coordination centers, facile surface functionalization, and tunable porosity enable widespread applications in environmental remediation and catalytic processes. Wu *et al.*[85] successfully modified PDI onto NH_2-MIL-88B(Fe, Mn) (FM88B) *via* water bath heating, forming a PDI/FM88B type-II heterojunction (Fig. 7f). This modification, confirmed by amide bond formation (Fig. 7g), enhanced structural stability and created an efficient interfacial electron transfer pathway. In the photo-Fenton system, 6%-PDI/FM88B achieved 89% tetracycline (TC) degradation under 30 min visible light (Fig. 7h). The performance enhancement arises from synergistic photocatalysis-Fenton processes, wherein the type-II heterojunction directs photoinduced electron transfer from PDI (donor) to FM88B (acceptor), while the interfacial IEF crucially promotes e^-–h^+ separation and directional migration – further amplified by the heterostructure's strong light absorption.

Despite demonstrating effective photogenerated charge segregation, it still exhibits limitations: (1) in type II heterojunctions, electrons transfer from the CB of the narrow-bandgap semiconductor to the CB of the wide-bandgap semiconductor, while holes migrate from the VB of the wide-bandgap to the VB of the narrow-bandgap semiconductor. This results in preserved carriers with both reduced redox potentials compared to the individual semiconductors. (2) The light absorption range of type II heterojunctions is fundamentally constrained

by the narrow-bandgap component, leading to inefficient broadband solar energy utilization. (3) In type II heterojunctions formed solely through physical contact, interfacial defects or gaps introduce additional charge-transfer resistance, significantly compromising carrier separation efficiency. (4) The preserved charge carriers with diminished redox potentials tend to accumulate and recombine in the absence of sacrificial agents for hole/electron consumption, ultimately degrading catalytic efficiency. Consequently, the type-II mechanism remains controversial.

3.3.2. **PDI-based Z-scheme heterojunction.** Z-scheme heterostructures exhibit fundamentally divergent charge transfer pathways compared to type-II configurations. Despite effectively improving carrier separation in these photocatalytic systems, oxidation–reduction processes in constituent semiconductors occur at diminished redox potentials, partially compromising their inherent redox capacity. Z-scheme photocatalysts have undergone three evolutionary stages of refinement, with Fig. 6a illustrating their progression from initial liquid-phase mediators to contemporary direct Z-scheme heterojunctions (Fig. 8a).[10,86,87] In 1979, Bard et al.[88] proposed the concept of liquid phase Z-scheme photocatalysis (Fig. 8b), which maximizes the redox potential of the heterojunction system, which can not only improve carrier separation, but also maintain strong redox capacity. However, the earliest Z-scheme architecture fundamentally differs from heterojunctions, comprising discrete semiconductor components interconnected by solution-phase redox mediators. This liquid-phase confinement restricts operational applicability, significantly limiting implementation

potential. The conceptual foundation for solid-state Z-scheme systems was established by Tada et al.[89] in 2006 (Fig. 8c), featuring two photocatalytic materials interlinked via solid electron-shuttling mediators. Upon light irradiation, semiconductors generate electron–hole pairs. In solid-state Z-scheme heterojunctions, electrons from semiconductor B's CB transfer to semiconductor A's VB through electron mediators (e.g., Pt, Au, Ag). This mechanism simultaneously accumulates holes with enhanced oxidation capability in semiconductor B's VB and electrons with heightened reduction capability in semiconductor A's CB. Consequently, spatial separation of photogenerated carriers is achieved while preserving strong redox potential. Furthermore, such solid-state Z-schemes function effectively across solid, liquid, and gaseous environments, significantly expanding their practical applicability.[90,91] However, achieving directional interfacial electron transfer remains fundamentally challenging. Concurrently, parasitic light absorption by common conductive mediators (e.g., Pt, Au, carbon materials) competes with primary catalytic components, necessitating further optimization of Z-scheme heterojunctions.[89,92] Based on the first and second generation Z-scheme heterojunctions, direct Z-heterojunctions have been proposed and widely used in photocatalysis (Fig. 8d). 2013 marked the introduction of tertiary-generation mediator-free Z-scheme heterojunctions by Yu et al.[93] comprising dual semiconductor components (PS I and PS II) with aligned band structures. These form ohmic interfacial contacts inherently containing defects that serve as recombination centers for PS II's CB electrons and PS I's VB holes. This ohmic interface inherently
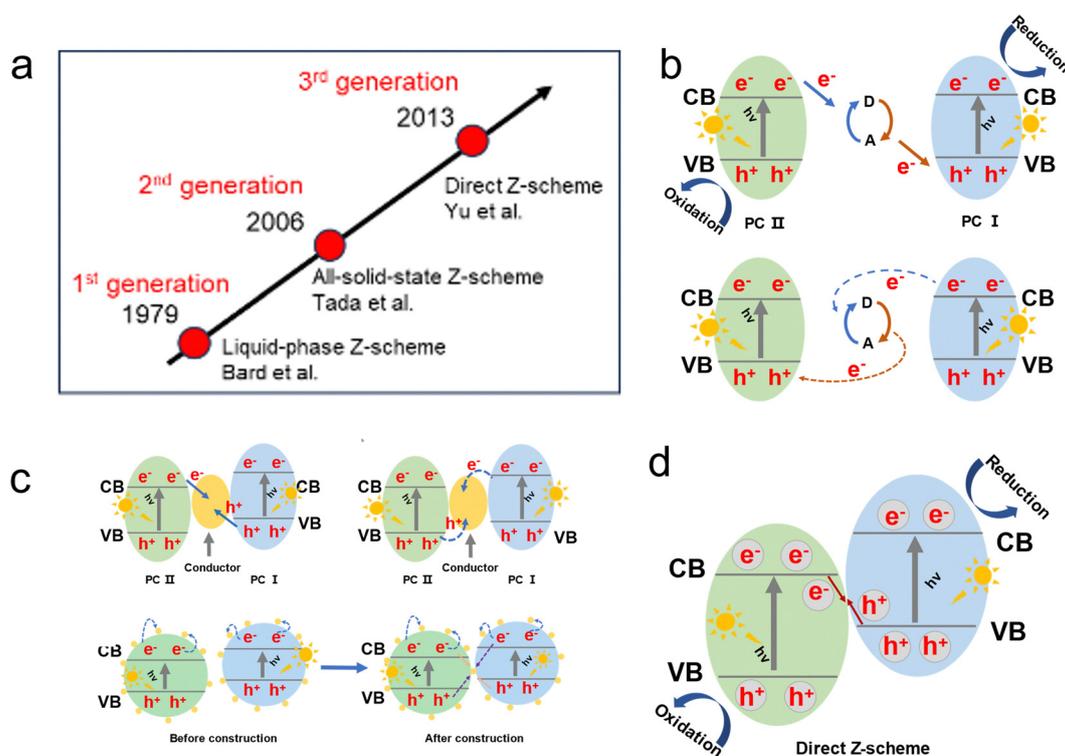

Fig. 8 (a) The first generation to the third generation Z-scheme photocatalytic system. (b) Liquid-phase Z-scheme heterojunction. (c) All-solid-state Z-scheme heterojunction. (d) Direct Z-scheme heterojunction.

contains defects that function as recombination centers for electrons from PS II's CB and holes from PS I's VB. Beyond inheriting advantages of prior Z-scheme generations, direct Z-schemes eliminate solid-state mediators, significantly reducing fabrication costs. Consequently, directional segregation of photo-induced charges is achieved while concurrently maintaining robust redox capability.[94] Recent advances extend Z-scheme architectures to PDI supramolecular systems. Constructing such heterojunctions can mitigate fundamental limitations of PDI's insufficiently negative CB potential while preserving its strong oxidative capacity from the more positive VB position.

For example, the π–π stacking in the NDINH/PDINH supramolecular system which was developed by Xu et al.[95] creates a giant IEF (Fig. 9a), significantly enhancing charge separation and carrier lifetime. This IEF drives a direct Z-scheme charge transfer pathway, preserving strong redox potentials for both half-reactions. Concurrently, the NDINH coating attenuates backscattered electromagnetic fields across PDINH surfaces, enhancing UV-light utilization efficiency. Exceptional full-spectrum photocatalytic overall water splitting (OWS) activity is enabled by these synergistic effects, achieving H_2 and O_2 evolution rates of 317.2 and 154.8 μmol g^{-1} h^{-1} respectively. This performance is further evidenced by a high O_2 evolution rate of 2.61 μmol g^{-1} h^{-1} (with $AgNO_3$) and 0.13% solar-to-hydrogen efficiency (Fig. 9b and c). Dai et al.[96] developed a 3D PANI/PDI direct Z-scheme photocatalytic system. Retained electrons in PANI's CB and holes in PDI's VB drove oxygen radical formation. Meanwhile, a novel PDI/FePc heterojunction featuring strong π–π interactions was synthesized via a self-assembled method[97] (Fig. 9d). This structure demonstrated enhanced visible-light photocatalytic degradation of tetracycline hydrochloride (TC), achieving removal rates 3-fold and

87.5-fold higher than pristine PDI and FePc, respectively and exhibiting superior oxidation kinetics, evidenced by a lower Tafel slope (131.1 mV dec^{-1}) versus PDI (228.6 mV dec^{-1}) (Fig. 9e and f). The observed boost originates from π-conjugated interactions minimizing layer-to-layer separation within the molecular assembly, consequently enhancing charge separation and transport efficiency.

3.3.3. PDI-based S-scheme heterojunction. Relative to conventional heterojunctions, Z-scheme architectures significantly enhance spatial segregation of photogenerated electron–hole pairs across distinct semiconductors. However, suboptimal interfacial charge transfer kinetics, compromised redox potentials of charge carriers, and limited photon harvesting efficiency collectively constrain photocatalytic performance enhancement in these systems.[98–100] Furthermore, inherent thermodynamic and kinetic constraints substantially limit the efficiency of conventional Z-scheme heterojunction photocatalysts. To overcome these limitations, the S-scheme (step-type) heterojunction theory, first proposed by Yu et al.,[101] pioneered the step-scheme (S-scheme) heterojunction concept, building upon direct Z-scheme architectures. This theoretical framework resolves fundamental ambiguities between traditional type-II and Z-scheme systems while addressing their intrinsic performance barriers. The system comprises two semiconductor materials functioning as a reduction photocatalyst (RP) and an oxidation photocatalyst (OP) respectively, featuring a staggered (type-II) band alignment where both the CB and VB of RP are positioned at higher energy levels than those of OP.[102] Under illumination, both semiconductors generate photogenerated electrons (e^-) and holes (h^+). Driven by the interfacial IEF and band bending, the less reductive electrons in the CB of OP recombine with the
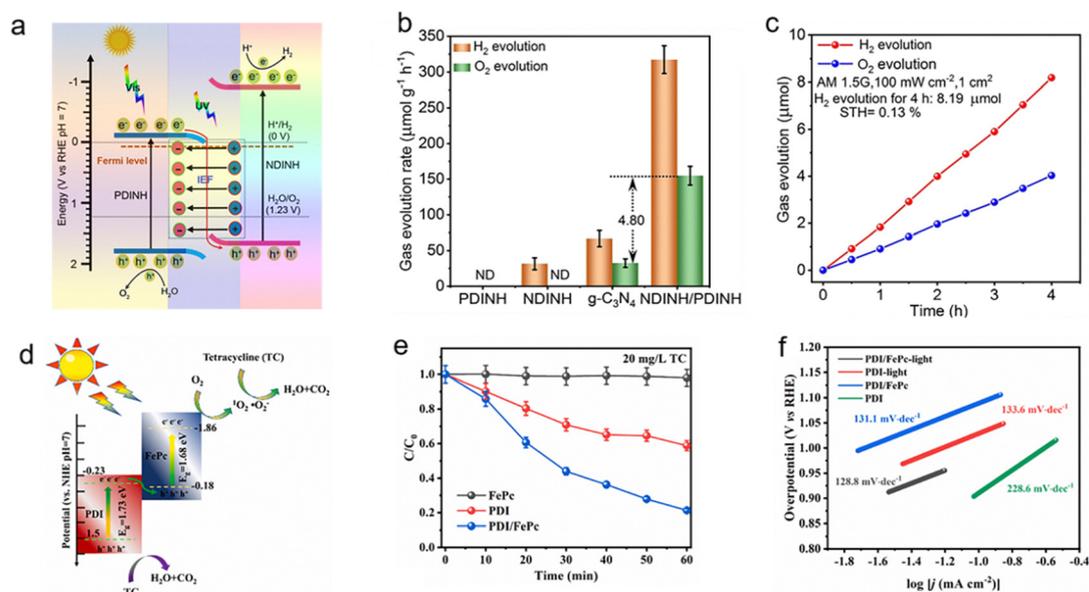

Fig. 9 (a) Schematic diagram of the NDINH/PDINH Z-scheme electron transfer process. (b) The overall water splitting performance over different catalysts under full-spectrum light irradiation. (c) Time course of photocatalytic overall water splitting over NDINH/PDINH. Reproduced from ref. 95. Copyright 2023, Wiley. (d) PDI/FePc Z-scheme electron transfer mechanism. (e) Photocatalytic degradation of TC activities over PDI, FePc and PDI/FePc heterojunctions. (f) The corresponding Tafel plots. Reproduced from ref. 97. Copyright 2023, Elsevier.

less oxidative holes in the VB of RP, while preserving the highly reductive electrons in the CB of RP and the strongly reductive holes in the VB of OP.[103] This mechanism achieves efficient charge separation while maintaining robust redox capabilities. The Fermi level alignment at the semiconductor junction induces electron migration from the higher-Fermi-level component to the lower-Fermi-level one, establishing an interfacial IEF with vector direction from RP to OP that promotes oriented charge carrier migration. For example, in the ZnTCPP/hBT hybrid system, the carboxyl groups (–COOH) of ZnTCPP form Ti–O–C covalent linkages with surface titanium atoms (Ti) of hBT. This chemical bonding enables intimate interfacial contact and establishes direct charge-transfer pathways between the components (Fig. 10).[102] Collectively, three synergistic mechanisms – IEF, band bending, and coulombic forces – drive selective recombination of OP's CB electrons and RP's VB holes. Consequently, less reactive carriers are eliminated while retaining high-energy electrons in RP's CB and holes in OP's VB for photocatalytic redox reactions.[101] The S-scheme heterojunction thereby: (1) enhances charge separation and reduces recombination; (2) maintains strong redox capability and enhances reaction activity; (3) enhances charge separation efficiency and broadens spectral response; (4) promotes interfacial stability. These attributes collectively boost photocatalytic activity and solar energy utilization efficiency.

Strategic engineering of electronic band gaps in hybrid organic–inorganic materials through covalent bonding enables precise fabrication of S-scheme heterojunctions. For example, through electrostatic interactions, the modification of PDI with Ag$_2$S nanoparticles by Yang et al.[104] was confirmed by TEM and HRTEM characterization, revealing uniform dispersion of Ag$_2$S on PDI surfaces with established heterojunction interfaces (Fig. 11b). The S-scheme Ag$_2$S/PDI heterojunction (Fig. 11a) exhibited superior photocatalytic activity, achieving 94% phenol degradation within 2 hours – significantly outperforming individual Ag$_2$S or PDI components (Fig. 11c). Due to its enhanced oxidation capability, the composite also facilitates in situ water oxidation for oxygen evolution. Chen et al.[105] fabricated an organic–inorganic dual S-scheme heterojunction In$_2$O$_3$/PDI/In$_2$S$_3$ (denoted IO/PDI/IS) photocatalyst through a synergistic approach combining solvent-induced self-assembly and electrostatic driving forces. The rational design leverages complementary band structures and an intensified IEF (Fig. 11e), enabling a defect-mediated dual S-scheme charge transfer pathway within the IO/PDI/IS architecture (Fig. 11d). This configuration demonstrates exceptional efficacy in degrading recalcitrant organic pollutants, including lignin and antibiotics. Notably, the system achieved an 80.9% mineralization rate for sodium lignosulfonate (SL), highlighting its advanced oxidative capability. Recently, Li et al.[106] developed an organic–inorganic S-scheme heterojunction photocatalyst by incorporating Nb^{5+}-substituted BiVO$_4$ (introducing oxygen vacancies, Ovs) with β-alanine-functionalized PDI supramolecules (Fig. 11f). This strategic modification reduced the bandgap and enhanced visible-light absorption. The composite demonstrated superior degradation efficiency for persistent aquatic pollutants including TC, RhB, SMX, and phenol. The enhanced photocatalytic activity stems from synergistic effects: Ovs facilitate charge separation, while interfacial Nb–O and Bi–O bonds maintain strong redox potentials (Fig. 11g).

In general, hybridizing PDI supramolecular photocatalysts with different semiconductors to form a heterojunction structure has shown to be an effective strategy mainly through extending the light absorption for photo-excitation and reducing the recombination of photo-generated carriers. However, to realize successful and reasonable construction of PDI-based heterojunction, several aspects need to be considered: (1) matched energy band potentials, allowing effective transfer and spatial separation for charge carriers from one semiconductor to another; (2) synthetic feasibility, adapted to PDI supramolecular photocatalysts' fabrication condition; (3) structure and activity stability, essential for their future application.

3.4. Metal deposition/doping and co-catalyst engineering

Depositing noble metals onto photocatalysts constitutes an effective approach for enhancing photocatalytic efficiency,[107] primarily through Schottky or Ohmic junction formation that modulates photogenerated charge transfer dynamics. Critically, plasmonic noble metal nanoparticles (e.g., Au, Ag, Cu) exploit localized surface plasmon resonance (LSPR) effects, wherein collective electron oscillations significantly boost photon absorption capacity.[108]

Miao et al.[109] fabricated PDI@Au NPs via electrostatic adsorption, demonstrating enhanced visible-light phenol photodegradation kinetics. This performance enhancement stems from synergistic effects: (1) Au nanoparticle surface plasmon resonance (SPR). (2) Resonance energy transfer (RET) with PDI collectively broadens visible-light utilization; (3) Au's lower Fermi level facilitates efficient electron–hole separation. For another
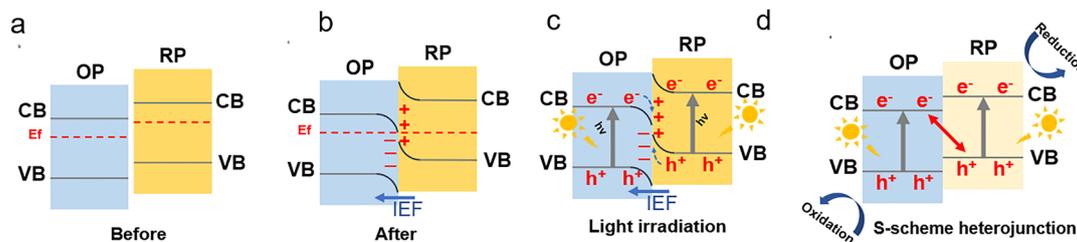

Fig. 10 (a)–(c) Charge-transfer processes in an S-scheme heterojunction. (a) Before contact, (b) after contact, and (c) photogenerated charge carrier transfer process under light irradiation. (d) S-scheme heterojunction.
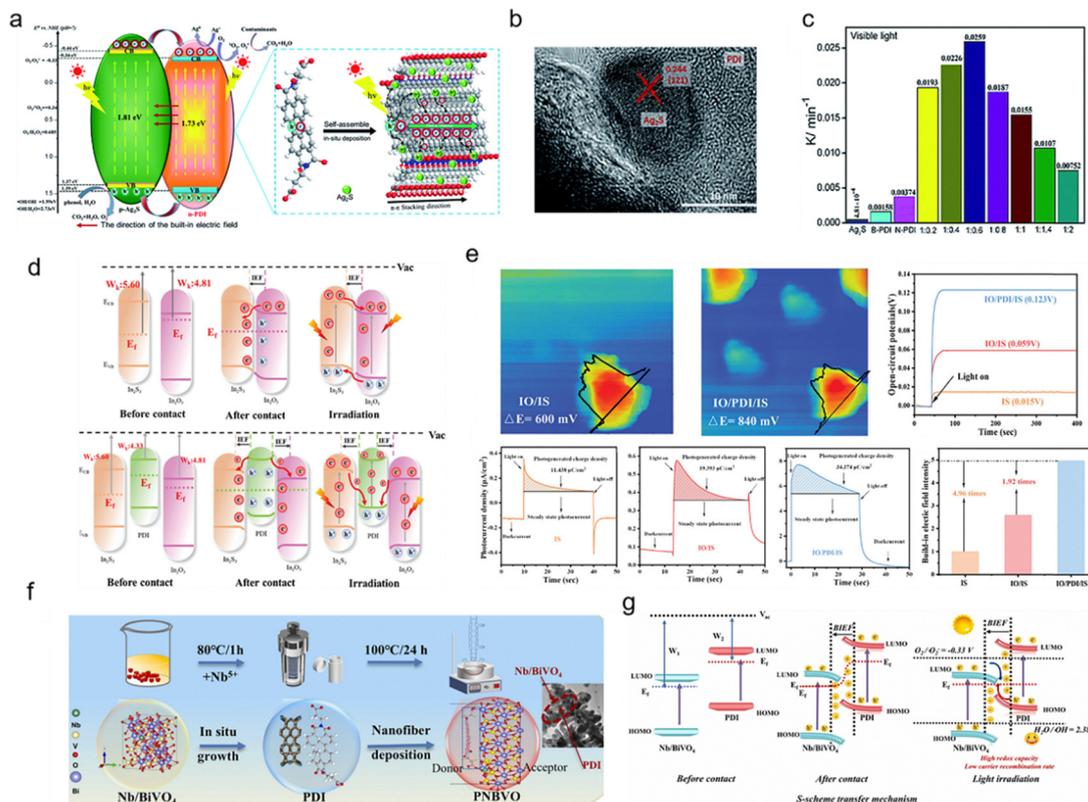
Fig. 11 (a) Mechanism of Ag_2S/PDI. (b) The HR-TEM image of Ag_2S/PDI (1 : 0.6). (c) Visible light irradiation (where B-PDI represents bulk-PDI, N-PDI represents nano-PDI, and 1 : x represents the mass ratio of Ag_2S to PDI). Reproduced from ref. 104. Copyright 2019, the Royal Society of Chemistry. (d) Schematic illustration of the charge migration between IO/IS and IO/PDI/IS. (e) The calculation of IEF intensity of IS, IO/IS and IO/PDI/IS. Reproduced from ref. 105. Copyright 2023, Wiley. (f) Schematic illustration of the facile solvothermal preparation of PNBVO composite materials. (g) Photocatalytic electron transfer mechanism of PNBVO. Reproduced from ref. 106. Copyright 2025, Elsevier.

example, Liu's group[110] achieved homogeneous deposition of platinum quantum dots (Pt QDs) on PDI supramolecular nanorods through a facile *in situ* reduction protocol (Fig. 12a). The optimized 1 wt% Pt QDs/PDI composite exhibited substantially enhanced photocatalytic activity, demonstrating 6.2-fold greater phenol degradation efficiency *versus* pristine PDI under visible light (Fig. 12b). Critically, the mild synthetic conditions preserved the nanorods' structural and electronic integrity. This performance enhancement stems from Pt QDs functioning as electron-shuttling mediators that efficiently capture and transfer photogenerated electrons, thereby accelerating charge separation kinetics.

Compared to metal deposits, metal doping enables atomic-level dispersion of active sites, preventing deactivation caused by metal particle agglomeration.[111,112] This strategy significantly increases the mass-specific density of catalytically active sites in the catalyst. For instance, Liang *et al.*[113] synthesized Cu-doped PDI supramolecules (CuPDIsm) with a 1D structure and integrated them with TiO_2 to form a heterojunction photocatalyst (Fig. 12c). Cu incorporation enhanced visible-light absorption and specific surface area. Crucially, Cu^{2+} coordination bridges and H-type π–π stacking significantly accelerated intramolecular electron transfer within CuPDIsm. Furthermore, photoinduced electrons migrated from CuPDIsm to TiO_2 *via* interfacial hydrogen bonding and electronic coupling, promoting charge separation. Consequently,

the TiO_2/CuPDIsm composite exhibited exceptional visible-light photodegradation activity, achieving 89.87% tetracycline and 97.26% methylene blue removal (Fig. 12d and e). Recently, Burcu Palas *et al.*[114] synthesized silver- and cobalt-doped PDI supramolecular photocatalysts and evaluated their efficacy for amoxicillin removal from aqueous solutions. Both bulk PDI and self-assembled PDI (SA-PDI) were functionalized with Ag or Co at 1 wt% and 10 wt% loadings (Fig. 12f). Photocatalytic reaction parameters were optimized at pH 4.6, a catalyst loading of 0.52 g L^{-1}, and an initial amoxicillin concentration of 10.3 mg L^{-1}. Under these visible-light conditions, the optimal system achieved 51.8% amoxicillin degradation efficiency (Fig. 12g).

3.5. Others

The hierarchical organization of PDI supramolecular systems is primarily mediated by π–π stacking, which dictates both structural integrity and optoelectronic properties. Intensified stacking interactions promote long-range π-conjugation and molecular orbital hybridization – key determinants for optimizing charge carrier mobility and separation efficiency in organic semiconductor architectures.[115] Based on the π–π stacking interactions in PDI supramolecular materials, researchers have integrated PDI with complementary π-conjugated organic systems to construct a larger π–π composite system. For example, Wei *et al.*[95] developed
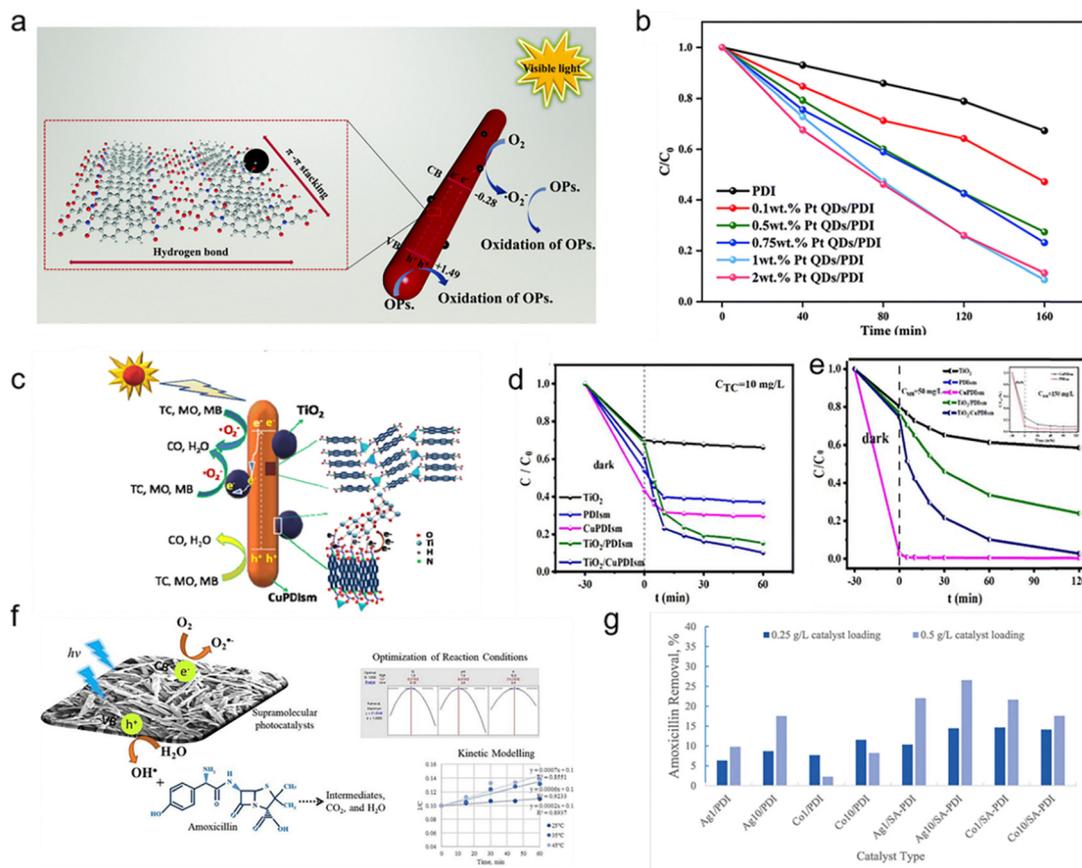
Fig. 12 (a) Diagram for the photocatalytic mechanism of Pt QDs/PDI. (b) Photocatalytic degradation performance of Pt QD/PDI composites. Reproduced from ref. 110. Copyright 2021, the Royal Society of Chemistry. (c) The photocatalytic mechanism of the TiO_2/CuPDIsm composite. (d) The photodegradation ratios of the samples toward TC. Reproduced from ref. 113. Copyright 2023, the Royal Society of Chemistry. (e) The photodegradation ratios of the samples toward MB. (f) The photocatalytic mechanism of the SA-PDI composite. (g) Amoxicillin removal performances of supramolecular catalysts in photocatalytic oxidation. Reproduced from ref. 114. Copyright 2023, Elsevier.

a π–π-stacked NDINH/PDINH supramolecular photocatalyst *via* rapid solution assembly. The strong intermolecular π-interactions induce a pronounced IEF and efficient charge transport. This optimized π-stacking configuration achieves full-spectrum overall water splitting with H_2/O_2 evolution rates of 317.2/154.8 μmol g^{-1} h^{-1} and exceptional 32-hour stability, demonstrating the pivotal role of π–π molecular engineering in photocatalyst design. Dai *et al.*[116] fabricated a 3D PANI/PDI heterojunction photocatalyst *via in situ* growth. The PANI framework enhances mechanical robustness and provides abundant reactive sites/mass transport pathways. Strong π–π interactions establish an extended delocalized π-system and favorable heterojunction, significantly promoting charge carrier separation. Consequently, tetracycline degradation rates increased 15.3- and 17-fold *versus* pristine PDI and PANI, respectively, with sustained activity over 75 h in continuous flow.

As a π-conjugated organic component, PDI supramolecular architectures can integrate with some other highly π-conjugated materials to build a π–π composite system to enhance interplanar coupling, and reduced stacking distances correlate with increased π-electron delocalization and orbital density superposition. These electronic configurations demonstrably facilitate charge carrier migration and separation, ultimately boosting photocatalytic efficiency and operational stability.

4. Photocatalytic application

Due to their high stability and narrow band gap, PDIs exhibit strong optical responses across the visible to near-infrared spectrum, enabling their widespread application in photocatalysis such as energy storage, energy conversion, and environmental protection. In this section, we present a succinct overview of their applications in photocatalytic water splitting, CO_2 reduction, N_2 fixation and pollutant degradation.

4.1. Water splitting

Photocatalytic technology plays a significant role in developing green energy and addressing energy and environmental challenges. In recent years, photocatalytic water splitting has attracted increasing attention in the global energy and environmental crisis due to its clean and environmentally friendly characteristics.[100,117–120] However, the widespread application of conventional inorganic photocatalysts (*e.g.*, TiO_2) is hindered

by limitations including poor visible-light utilization, low quantum yield, and high cost.[121] To overcome these constraints, the development of novel, efficient photocatalytic materials is actively pursued. Notably, PDI-based photocatalysts have rapidly emerged as a research focus, particularly for photocatalytic water splitting. Their prominence stems from exceptional light-harvesting capacity, high electron mobility, robust chemical and photochemical stability, and the unique ability to precisely tailor band structures and surface properties through molecular engineering.

4.1.1. H$_2$ production. The rapid progression of modern society faces major energy challenges due to rising consumption and depletion of fossil fuel sources. Converting abundant solar energy into chemical fuels like H$_2$ is therefore of significant interest. Photocatalytic water splitting under sunlight irradiation using a photocatalyst for H$_2$ production represents an effective approach to addressing energy and environmental issues.[86,122] Thermodynamically, active photocatalysts require a CB edge more negative than the H$^+$/H$_2$ reduction potential (0 V vs. NHE, pH = 0) and a VB edge more positive than the O$_2$/H$_2$O oxidation potential (1.23 V vs. NHE, pH = 0). Most PDI-based photocatalysts, with a CB around -0.8 to -0.1 eV vs. NHE,[62,123,124] are thus widely studied for photocatalytic H$_2$ production. Their H$_2$ production activities are summarized in Table 3 for comparison.

However, the photocatalytic H$_2$ production performance of pure PDIs is severely limited by inherent challenges including unfavorable band structure, rapid charge-carrier recombination, insufficient surface active sites, and mass transfer constraints.[62,125] To address these limitations, modification strategies such as side chain regulation, elemental doping, and heterojunction construction are commonly employed to significantly enhance their photocatalytic activity.

Constructing heterojunctions is a common strategy to enhance PDI-based photocatalytic hydrogen production. This approach can effectively promote the separation and transfer of photogenerated electron–hole pairs through the IEF formed at the heterojunction interface, reduce the recombination probability of carriers, and extend their lifetime. Additionally, heterojunctions can broaden the light absorption range of PDI-based materials, allowing them to harvest more solar energy and further boost the photocatalytic hydrogen production performance. For example, Zhu and co-workers[126] designed a novel co-assembled material for photocatalytic H$_2$ production through π–π stacking interactions of TPPS/PDI organic semiconductors with a D–A interface (Fig. 13a and b). The TPPS/PDIs exhibit a remarkable photocatalytic H$_2$ production rate of 30.36 mmol g^{-1} h^{-1}, attributed to its pronounced IEF that facilitates efficient charge separation and a giant

Table 3 Summary of the photocatalytic activity of PDI-based photocatalysts

Photocatalyst	Application	Light source	Amount of catalyst	Photocatalytic performance	AQY	Ref.
P-PMPDI	H$_2$ production	300 W Xe lamp, $\lambda > 420$ nm	50 mg	1170 μmol g^{-1} h^{-1}	2.96 (550 nm)	62
Zn$_{0.5}$Cd$_{0.5}$S/PDIs	H$_2$ production	Solar simulator (AM 1.5)	50 mg	1320 μmol g^{-1} h^{-1}	—	124
PDI-phthalic	H$_2$ production	300 W Xe lamp, $\lambda > 420$ nm	25 mg	1100 μmol g^{-1} h^{-1}	—	69
N-APDIs	H$_2$ production	500 W Xe lamp, $\lambda > 420$ nm	20 mg	61 490 μmol g^{-1} h^{-1}	5.9 (420 nm)	127
S-APDIs	H$_2$ production	Hg lamp, 500 W	20 mg	900 μmol g^{-1} h^{-1}	—	132
g-C$_3$N$_4$/PDIs	H$_2$ production	300 W Xe lamp, $\lambda > 420$ nm	10 mg	1600 μmol g^{-1} h^{-1}	—	176
TATF-COF/PUP	H$_2$ production	350 W Xe lamp, $\lambda > 420$ nm	5 mg	94 500 μmol g^{-1} h^{-1}	19.7 (420 nm)	177
GQDs/PDIs	H$_2$ production	500 W Xe lamp, $\lambda > 420$ nm	25 mg	1600 μmol g^{-1} h^{-1}	0.5 (420 nm)	178
P-PMPDIs-Zr	H$_2$ production	300 W Xe lamp, $\lambda > 420$ nm	50 mg	504 600 μmol g^{-1} h^{-1}	11.7 (420 nm)	125
CN-PDI	H$_2$ production	450 nm LED light source	5 mg	17 700 μmol g^{-1} h^{-1}	5.8 (450 nm)	179
TiO$_2$/PDIs	H$_2$ production	300 W Xe lamp, $\lambda > 420$ nm	50 mg	97 700 μmol g^{-1} h^{-1}	—	180
g-C$_3$N$_4$/Pt/PDIs	H$_2$ production	400 W Xe lamp, $\lambda > 420$ nm	25 mg	150 μmol g^{-1} h^{-1}	0.31 (420 nm)	181
PDIs/TiO$_2$	H$_2$ production	300 W Xe lamp, $\lambda > 365$ nm	100 mg	1200 μmol g^{-1} h^{-1}	70.69 (365 nm)	182
PDI-NH	O$_2$ production	300 W Xe lamp, (420 nm cutoff filter)	15 mg	40.6 mmol g^{-1} h^{-1}	10.4 (400 nm)	132
p-Ag$_2$S/n-PDI	O$_2$ production	500 W xenon lamp, 420 nm cut-off filter	25 mg	34 μmol g^{-1} h^{-1}	—	104
Oxamide-PDI	O$_2$ production	300 W full-spectrum xenon lamp, (783 mW cm^{-2})	0.025 g	5110.25 μmol g^{-1} h^{-1}	2.15 (420 nm)	77
PDI/Co$_3$O$_4$/Pt	O$_2$ production	300 W Xe lamp, 420 nm cut-off filter	15 mg	24.4 mmol g^{-1} h^{-1}	6.9 (420 nm)	133
PT-CB	O$_2$ production	300 W Xe lamp, (420 nm cut-off filter)	5 mg	966.28 μmol g^{-1} h^{-1}	—	183
3D MXene/GO/PDI	CO$_2$ reduction	350 W xenon lamp for UV-vis irradiation	10 mg	711 μmol g^{-1} h^{-1} (HCHO)	—	142
3%Au/PHI-PDI	CO$_2$ reduction	300 W Xe lamp	30 mg	122.65 μmol g^{-1} h^{-1}(CO)	—	143
Cu@PDI(30%)-NZU67	CO$_2$ reduction	300 W Xe lamp UV cut-off filter ($\lambda > 420$ nm)	50 mg	941.28 μmol g^{-1} h^{-1} (ETHO)	—	147
BOPDI	N$_2$ fixation	300 W Xe lamp ($\lambda > 420$ nm)	20 mg	74 μmol g^{-1} h^{-1}	1.29 (450 nm)	159
PDIMA-2	N$_2$ fixation	300 W Xe lamp ($\lambda > 400$ nm)	20 mg	49.9 μmol g^{-1} h^{-1}	1.07 (420 nm)	160
30% PDI/10H-CNv	N$_2$ fixation	300 W xenon lamp, simulating sunlight (AM 1.5G)	10 mg	519.2 μmol g^{-1} h^{-1}	—	161
3D PANI/PDI	TC removal	5 W LED lamp, (420 nm cut-off filter)	25 mg	0.5265 h^{-1}	—	116
CNPDI	TC removal	250 W xenon lamp, (420 nm cut-off filter)	—	0.026 min^{-1}	—	178
I-PDI/PEDOT-M	TC removal	250 W xenon lamp	20 mg	0.0087 min^{-1}	—	170
FM88B	TC removal	300 W xenon lamp $\lambda > 420$ nm	7 mg	0.067 min^{-1}	—	85
BN/PDI-2-350	TC removal	Visible light, xenon lamp	15 mg	—	—	184
PDI (5.0%)/BiOCl-BiPO$_4$	RhB/TC removal	Visible light irradiation	25 mg	0.037 min^{-1}/0.0135 min^{-1}	—	185
MNP30/PDS/Vis	SMX removal	300 W xenon lamp, cut-420 nm filter	—	0.8873 min^{-1}	—	186
BWGP-2	BPA removal	300 W Xe lamp	—	55%	—	187

interfacial potential gradient that extends the lifetime of photo-excited carriers. To broaden the absorption spectrum and enhance the separation of photoinduced charges, Yang *et al.*[104] reported the fabrication of p-Ag$_2$S/n-PDIs *via* a synergistic strategy combining hydrogen bonding, π–π stacking interactions, and a two-step electrostatic self-assembly process (Fig. 13c). Ag$_2$S enhances π–π orbital overlap in PDI assemblies, facilitating directional photoelectron transport along the 1D π-conjugated pathways. Concurrently, Ag$_2$S extends the visible-light harvesting capacity, thereby promoting photochemical conversion efficiency. Finally, p-Ag$_2$S/n-PDIs heterojunctions exhibit superior ultraviolet-light, visible-light and full spectrum photocatalytic performance.

In the context of the water splitting reaction mechanism, the suppression of electron–hole recombination emerges as a pivotal factor for enhancing photocatalytic activity. Additionally, both metal and non-metal element doping strategies have been demonstrated to effectively boost the photocatalytic H$_2$ production performance of PDIs, thereby offering promising avenues for optimizing their catalytic efficiency in energy conversion systems. For example, the metal-doped supramolecular P-PMPDI-Zr[125] exhibited exceptional hydrogen evolution activity under visible light irradiation, achieving a remarkable rate of 50.46 mmol g^{-1} h^{-1}, which is 4.34 times higher than that of the Zr-free cationic counterpart. Notably, P-PMPDI-Zr maintains substantial photocatalytic activity even at longer wavelengths, demonstrating an apparent quantum yield (AQY) of 11.70% at 630 nm, along with excellent stability. These results highlight that metal doping serves as a facile and effective strategy to broaden the absorption

spectrum and enhance charge transfer in supramolecular systems. Furthermore, doping with Co, Ni, and Cu also significantly improves the HER performance compared to pristine P-PMPDI, further validating the universality of this approach. Xu *et al.*[127] successfully incorporated non-metallic elements N, S, and Se into PDIs (polyimide derivatives), yielding N-APDI, S-APDI, and Se-APDI samples. These heteroatom-annulated PDI supramolecules exhibited a substantially higher H$_2$ production compared to non-annulated APDI counterparts. Mechanistically, this enhanced photocatalytic activity is attributed to two key factors (Fig. 13d). The incorporation of heteroatoms strengthens the molecular dipole moment, thereby intensifying the IEF to facilitate the separation and migration of photogenerated charge carriers. Simultaneously, heteroatom annulation generates additional active sites that optimize the hydrogen evolution reaction (HER) kinetics, promoting more efficient H$_2$ production.

The fabrication of a PDI heterojunction also presents a dual-pronged advantage: it enhances the efficiency of charge separation and maintains the strong redox capability of photocatalysts, thereby realizing efficient photocatalytic hydrogen generation. For example, Yu and co-workers[128] successfully designed an inorganic–organic S-scheme heterojunction. As illustrated in Fig. 14a, ZIS nanosheets are grown onto the disc-shaped MIL-125-PDI surface, forming unique hollow nanodiscs with a hierarchical architecture. This configuration endows the material with abundant surface active sites, a tailored electronic structure, and a spatially segregated redox interface. Experimental results and theoretical calculations consistently indicate that the staggered band alignment and work function disparity between
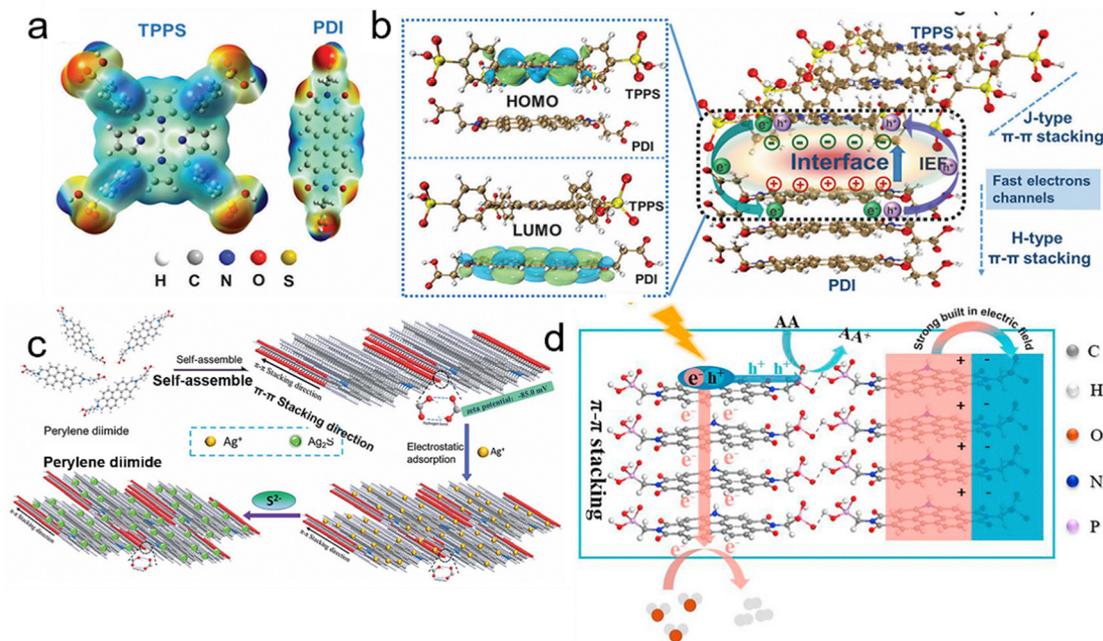

Fig. 13 (a) The molecular formula and electrostatic potential distribution of TPPS and PDI. (b) Left: The frontier molecular orbital distribution of TPPS and PDI at the interface; right: schematic diagram of interfacial interactions of co-assembly supramolecular TPPS/PDI. Reproduced from ref. 126. Copyright 2022, Wiley. (c) Schematic illustration of the synthesis of the self-assembled PDI and Ag$_2$S/PDI composite. Reproduced from ref. 104. Copyright 2019, the Royal Society of Chemistry. (d) Proposed electron transfer mechanism of supramolecular R-APDI for photocatalytic H$_2$ production. Reproduced from ref. 127. Copyright 2022, Elsevier.
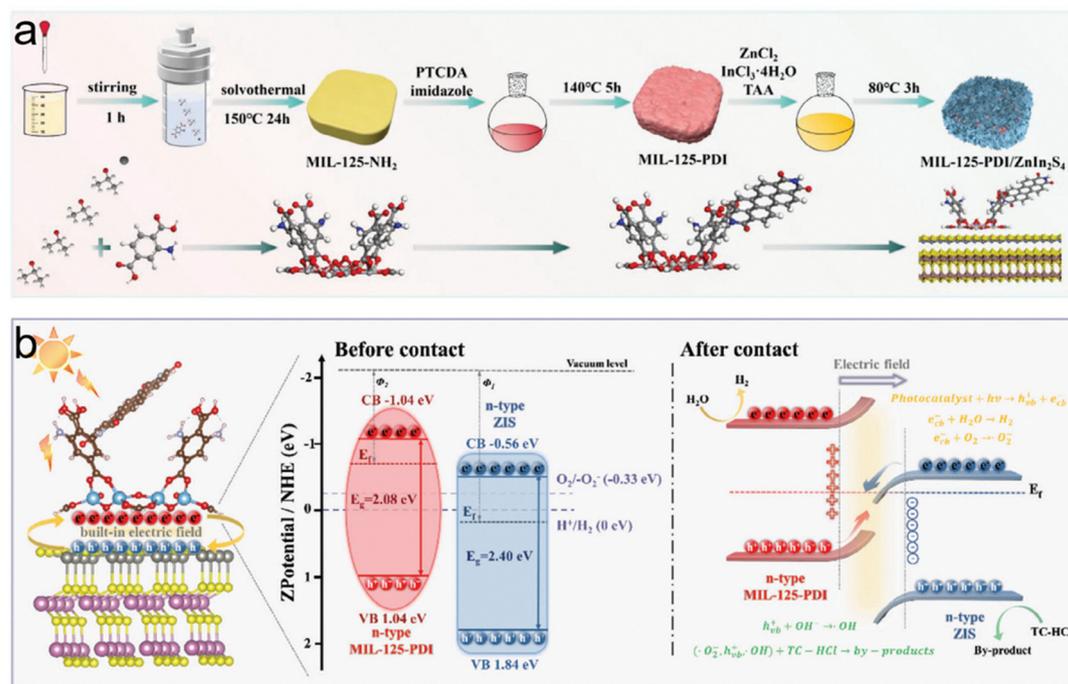
Fig. 14 (a) Synthetic route for MIL-125-PDI/ZIS. (b) Schematic of the proposed mechanism of charge transfer over MIL-125-PDI/ZIS under simulated sunlight irradiation. Reproduced from ref. 128. Copyright 2024, Wiley.

MIL-125-PDI and ZIS give rise to the formation of an IEF. This electric field, in turn, governs the pathways of charge transfer and consequently improves the efficiency of charge separation (Fig. 14b).

4.1.2. O$_2$ production. The water oxidation reaction is an essential semi-reaction for photocatalytic water splitting. However, due to the four-electron transfer reaction, water oxidation becomes the rate-determining step. Photocatalytic water oxidation, a critical half-reaction for overall water splitting, remains a kinetic bottleneck due to its demanding four-electron transfer process. The scarcity of efficient catalysts and inherently slow reaction kinetics impede progress toward large-scale applications. Emerging organic semiconductors – notably graphitic carbon nitride (g-C$_3$N$_4$),[129] PDIs,[130] and COFs[131] – offer promise through tunable band structures and thermodynamic feasibility for water splitting. In particular, PDI-based photocatalysts exhibit sufficiently deep VBs (+1.6 to +2.1 V *vs.* NHE)[71] to thermodynamically drive water oxidation. However, poor charge separation efficiency limits their oxygen evolution rates. Therefore, the development of PDI photocatalysts with high O$_2$ production ability is crucial through water splitting. Recent advances in PDI photocatalyst design (*e.g.*, heterojunction engineering, polymer modulation, molecular engineering of PDI monomers and co-catalysts) have significantly improved photocatalytic oxygen production. This section summarizes key developments in high-performance PDI materials for O$_2$ generation, with comparative metrics detailed in Table 3.

Heterojunction engineering represents a key strategy for establishing robust IEFs, which drive directional charge migration to overcome kinetic bottlenecks in photocatalytic O$_2$ evolution by spatially isolating redox sites. For instance, Yang *et al.*[104] successfully constructed an efficient full-spectrum responsive p-Ag$_2$S/n-PDI heterojunction with a photocatalytic O$_2$ production rate of about 34.6256 mmol g^{-1} h^{-1} (Fig. 15a and b). The enhanced photocatalytic performance can be primarily ascribed to several key factors facilitated by Ag$_2$S: firstly, it optimizes the π–π stacking degree within PDI, significantly improving the mobility of photo-generated electrons along the quasi-one-dimensional stacking channels. Secondly, Ag$_2$S broadens light absorption, thereby boosting the conversion efficiency of light into chemical energy. Furthermore, the intrinsic IEF formed at the Ag$_2$S/PDI interface favors the efficient separation of photo-induced charge carriers. This synergistic effect, coupled with the formation of a p-Ag$_2$S/n-PDI heterojunction, generates a greater quantity of active species compared to pristine PDI, ultimately leading to a substantially enhanced oxidation capability.

Nowadays, enhancing the crystallinity of PDIs during their molecular assembly *via* non-covalent interactions represents a critical strategy for boosting photocatalytic efficacy. This crystalline ordering facilitates efficient charge carrier transport by augmenting the intrinsic IEF. For example, Zhu *et al.*[132] synthesized a highly crystalline PDI supramolecular photocatalyst (PDI-NH) *via* an imidazole solvent method (Fig. 15c). The catalyst exhibits a breakthrough oxygen evolution rate with high apparent quantum yield, which is 1353 times higher than the low crystalline PDI-NH (Fig. 15d). This crystallinity originates from ordered self-assembly *via* π–π stacking and hydrogen bonding within the molten imidazole.

PDI supramolecular assembly, held together by weak non-covalent interactions, often suffer from poor structural stability.
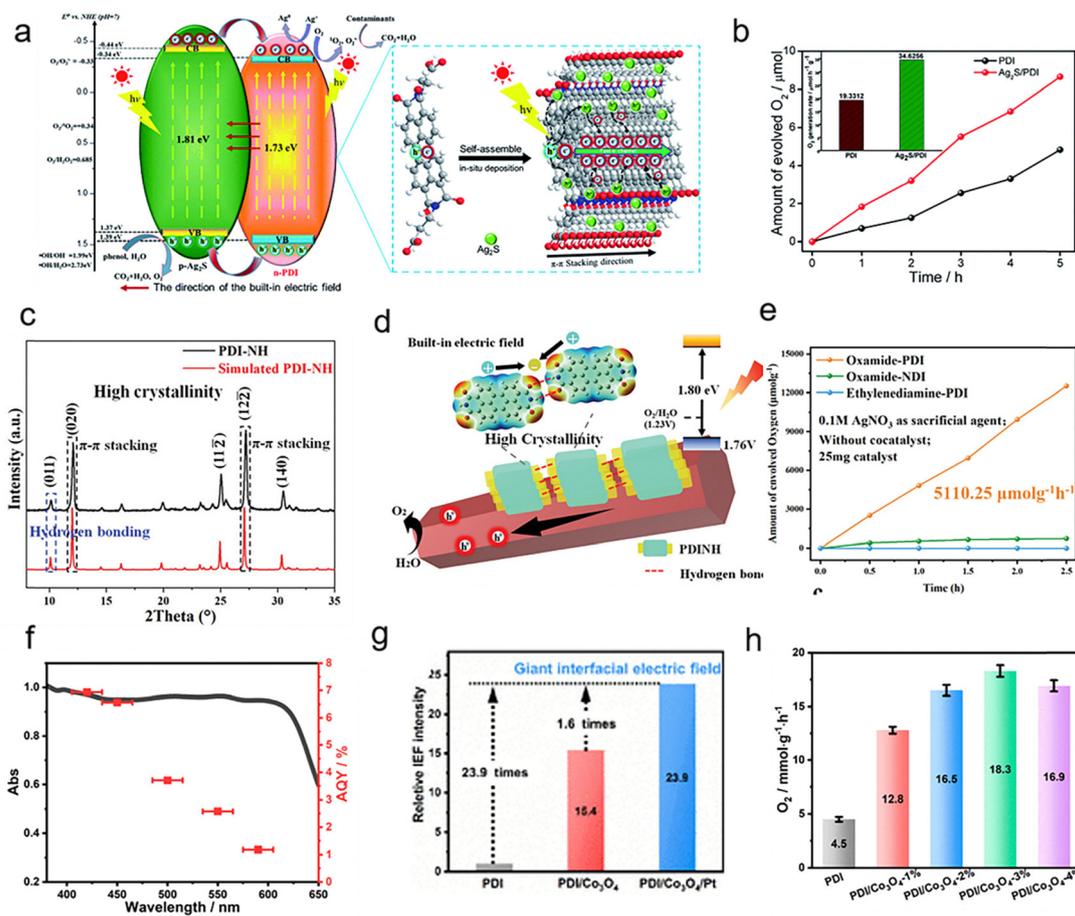
Fig. 15 (a) The synthesis of the self-assembled PDI and Ag$_2$S/PDI composite. (b) Amount of O$_2$ evolved by Ag$_2$S/PDI. Reproduced from ref. 104. Copyright 2019, the Royal Society of Chemistry. (c) XRD spectrum of PDI-NH. (d) Schematic illustration of PDI-NH. Reproduced from ref. 132. Copyright 2022, Wiley. (e) Amount of O$_2$ evolved by oxamide-PDI. Reproduced from ref. 77. Copyright 2023, Wiley. (f) AQY, (g) relative IEF and (h) amount of O$_2$ evolved by PDI/Co$_3$O$_4$/Pt. Reproduced from ref. 133. Copyright 2023, American Chemical Society.

Therefore, designing PDI polymers is another efficient strategy to improve the O$_2$ production rate. Liu's group[77] synthesized a highly-crystallized linear conjugated polymer, Oxamide-PDI, by alternating copolymerization of PTCDA with hydrophilic oxamide. The more extended π-conjugation of perylene-cored PTCDA endows oxamide-PDI with a larger value of interaction energy for π–π stacking. Featuring a planar perylene core with extended conjugation and a polar dicarbonyl bridging group, oxamide-PDI formed rigid 1D ordered stacks. This structure endowed exceptional π–π stacking-mediated exciton splitting and robust intramolecular charge transfer capabilities through the bridging group. Notably, the highly crystalline oxamide-PDI achieved remarkable solar-driven O$_2$ evolution efficiency under mild pH conditions without co-catalysts (Fig. 15e).

A notable aspect of the aforementioned research is its demonstration of efficacy in the absence of oxygen evolution reaction (OER) co-catalysts. Nevertheless, the strategic incorporation of such co-catalysts remains highly advantageous, as they facilitate the extraction and trapping of photogenerated charges, furnish additional redox-active sites, and reduce both the reaction overpotential and activation energy barrier associated with surface oxygen evolution. Consequently, the strategic design of efficient semiconductor/co-catalyst composite materials represents an essential approach for enhancing photocatalytic performance in the OER. Li et al.[133] constructed a dual cocatalysts-modified PDI polymer (PDI/Co$_3$O$_4$/Pt) for facilitating photocatalytic O$_2$ evolution performance to improve the solar utilization. The Co$_3$O$_4$, acting as superior active sites, contributed to lower the barrier of the water oxidation reaction, and the IEFs of cocatalysts and PDI drive separation and transfer of photogenerated charges. As a consequence, DI/Co$_3$O$_4$/Pt exhibited strong stability and a photocatalytic O$_2$ evolution rate of 24.4 mmol g^{-1} h^{-1}, which is 5.4 times higher than that of pure PDI. The apparent quantum yield of the O$_2$ evolution reaction reaches 6.9% at 420 nm and remains 1.2% at 590 nm. In the system, Co$_3$O$_4$ provides the dominant effects for photocatalytic O$_2$ evolution reactions, and Pt mainly plays a role in charge transfer (Fig. 15f and g).

4.2. CO$_2$ reduction

The photocatalytic conversion of CO$_2$ and water into chemicals and fuels using light energy, emulating natural photosynthesis, is considered to be among the most promising methods for decreasing atmospheric CO$_2$ levels.[134–137] Induced photosynthesis via the

photocatalytic CO_2 reduction reaction (CO_2RR) to value-added chemicals is a long-lasting way to address energy and ecological problems.[138–140] The oxidative half-reaction in photocatalytic systems predominantly involves water oxidation to generate oxygen (O_2) or hydrogen peroxide (H_2O_2). Despite the inherent merits of CO_2 photocatalytic conversion technology, its practical implementation confronts significant challenges. It is still a multi-step process demanding the concurrent fulfilment of both thermodynamic and kinetic criteria. Thermodynamically, the redox potentials of the reaction intermediates must align favorably with the band edge positions of the photocatalyst. Kinetically, the substantial energy barriers associated with multi-electron transfer processes must be overcome. Consequently, an efficient photocatalyst for the overall reduction of CO_2 necessitates both exceptional photogenerated charge separation efficiency and appropriately positioned conduction band minimum and valence band maximum to drive the reduction and oxidation half-reactions, respectively. Therefore, developing highly active photocatalytic systems is crucial for enhancing the reaction rate of photocatalytic CO_2 reduction. Compared to inorganic semiconductors, organic semiconductors offer distinct advantages, including chemically tunable optoelectronic properties, robust photochemical and thermal stability, adjustable band energy levels, flexible morphological and structural design, facile synthetic modulation, and elemental abundance. Among diverse organic semiconductors, PDI exhibits a broad spectral response range, environmental benignity, and low cost, leading to its widespread application in fields such as fluorescent probes, sensors, transistors, and photocatalytic systems.

For example, Hu and co-workers[141] engineered ZrO_2-supported PDI photosensitizers via salicylic acid anchors (Fig. 16a). Coupled with Re(bpy)(CO)$_3$Cl/TEOA in DMF, the composite demonstrated competitive CO_2-to-CO TONs under white LED (100 mW cm^{-2}), attributed to stable surface grafting and facilitated electron transfer at minimal catalyst usage (Fig. 16b and c). The strong anchoring of salicylic acid on the surface of ZrO_2 and efficient electron transfer at low catalyst concentrations make ZrO_2/PDIs a promising candidate for CO_2 photoreduction applications.

While the VB position of PDI offers a strong oxidation capability, the positive CB potential results in an insufficient thermodynamic driving force for reduction. Furthermore, rapid recombination of photogenerated charge carriers significantly limits the practical application of PDI. Consequently, PDI-based heterojunction engineering overcomes this limitation through two synergistic mechanisms: (1) tailored energy band alignment and (2) optimized photogenerated carrier separation, ultimately boosting CO_2-to-fuel conversion efficiency when utilizing H_2O as the reductant. For example, Wu et al.[142] fabricated novel 3D MXene/GO/PDI aerogels via self-assembly (Fig. 16d), establishing an electron transfer network through π–π stacking that enhanced electron delocalization. The optimized aerogel achieved a formaldehyde (HCHO) production rate of 771.1 μmol g^{-1} h^{-1} in photocatalytic CO_2 reduction, an 8-fold enhancement over MXene/PDI (Fig. 16e and f). Characterization confirmed a strongly coupled interface via π–π cross-linking, generating a robust IEF and narrowed

bandgap. Concurrently, a Z-scheme heterojunction formed between MXene/GO and PDI due to their aligned band structures. This dual configuration accelerated photogenerated electron transfer and enhanced interfacial redox capabilities.

Non-covalent heterojunctions, characterized by the absence of robust chemical bonding, typically exhibit compromised interfacial carrier transport efficiency. This limitation adversely impacts photocatalytic CO_2 reduction performance. In contrast, covalently bonded heterojunctions feature strong covalent linkages between semiconductor components, providing directional charge transfer channels that enhance photocatalytic activity. Yang et al.[143] constructed Au/PHI-PDI with synergistic junctions: (1) covalent S-scheme heterojunction enabling rapid intralayer charge transfer via PHI-PDI bonds, and (2) Schottky junction creating vertical IEF for interlayer charge transport (Fig. 16g). The covalent connection between PHI and PDI constructs a fast charge transfer channel, which is beneficial to boost intralayer charge separation and migration. Furthermore, the formed Schottky junction could generate a vertical IEF, which enhances interlayer charge transport (Fig. 16h and i). As a result, this architecture boosted charge utilization efficiency, yielding 122.65 μmol g^{-1} h^{-1} CO over 3%Au/PHI-PDI surpassing PHI-PDI and PHI by factors of 2.77 and 9.24 respectively.

Currently, the integration of PDI with organic frameworks has also begun to be investigated in the field of photocatalytic CO_2 reduction, such as in metal–organic frameworks (MOFs), covalent organic frameworks (COFs), etc. For example, research on MOFs containing PDI has focused on applications in sensing[144] and photocatalytic degradation,[145,146] and few studies have studied their potential for CO_2 conversion. Recently, Altalbawy and co-workers[147] incorporated a PDI chromophore moiety into a Cu@PDI(30%)-NZU67 and applied the resulting material for CO_2 conversion of ETHO for the first time (Fig. 16j–l). From a MOF engineering perspective, anchoring PDI within secondary building units (SBUs) proved strategically superior to conventional linker-based integration. For another, Zhu and colleagues[148] developed a cobalt-metalated, one-dimensional covalent organic framework with ABC stacking (PP-COF-Co). This framework integrates PDI as a photosensitizing unit and 1,10-phenanthroline moieties as metal-coordinating sites which exhibit a 57-fold increase in photocatalytic CO_2 reduction activity compared to its pristine analogue.

4.3. N$_2$ fixation

Ammonia (NH_3) serves as an essential industrial chemical for manufacturing explosives and fertilizers, underpinning critical societal infrastructure.[149–151] Conventionally, industrial-scale NH_3 production employs the Haber–Bosch process, where Fe-based catalysts mediate N_2 and H_2 conversion under elevated temperatures and pressures,[152–155] with an annual global energy consumption of ∼2% and responsibility for 1.6% of anthropogenic CO_2 emissions.[156,157] Photocatalytic nitrogen reduction reaction (PNRR) represents an emerging sustainable alternative to the conventional Haber–Bosch process. However, the exceptionally strong nonpolar N≡N triple bond in N_2 molecules possesses significant challenges for efficient photocatalytic
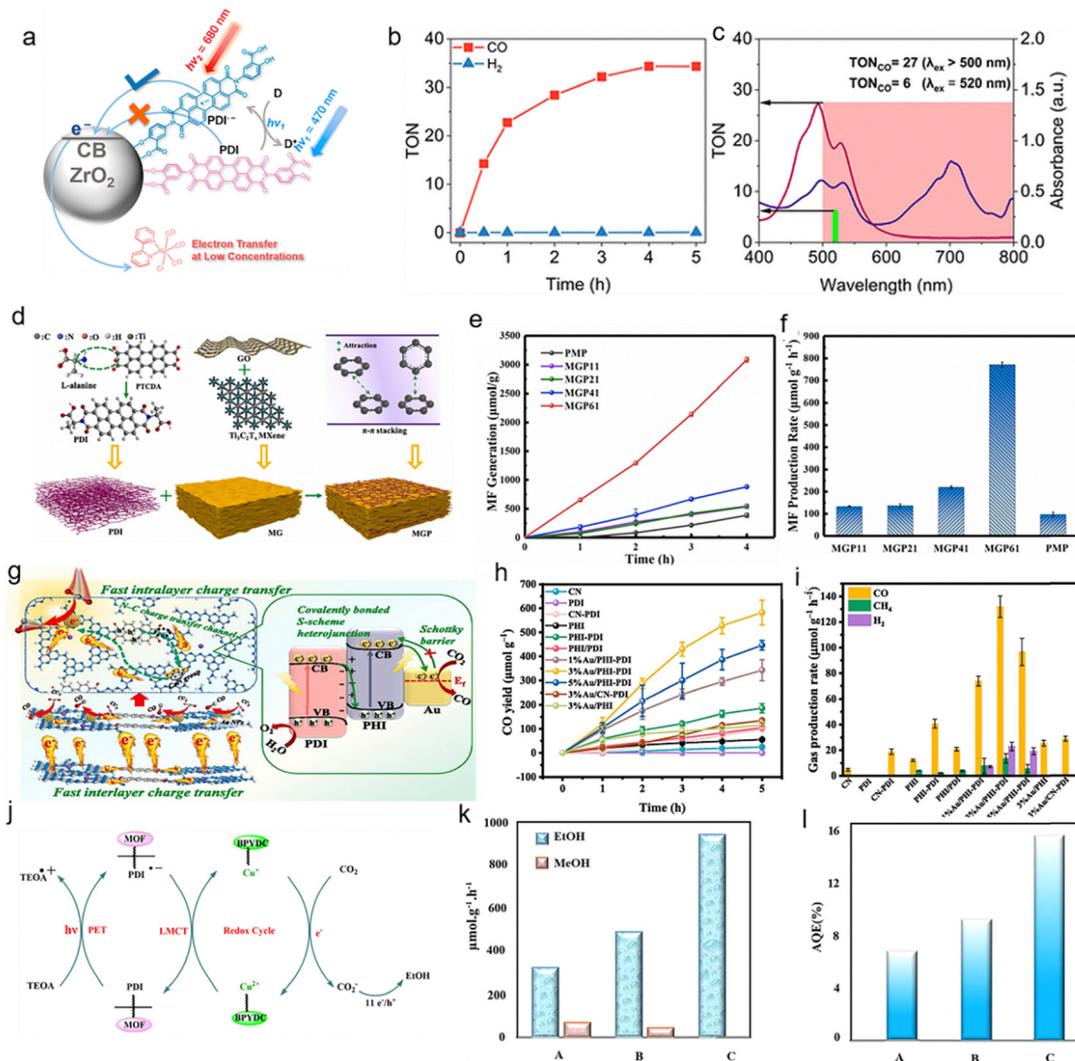
Fig. 16 (a) Strategy for photogeneration of a potent and long-lived $ZrO_2(e^-)$. (b) TON of CO and H_2 by Re(bpy)(CO)$_3$Cl and ZrO_2|PDI as a function of irradiation time. (c) Photocatalytic CO_2 reduction TON under 520 nm irradiation or broad band irradiation with wavelengths greater than 500 nm. Reproduced from ref. 141. Copyright 2022, American Chemical Society. (d) Schematic illustration of the MXene/GO/PDI composite aerogels. (e) MF generation yield of samples changing over time under the irradiation for 4 h. (f) MF generation rate of samples under the irradiation for 4 h. Reproduced from ref. 142. Copyright 2022, Elsevier. (g) Proposed photocatalytic mechanism for Au/PHI-PDI. (h) Time-dependent CO evolution performances. (i) Stability test over the 3%Au/PHI-PDI. Reproduced from ref. 143. Copyright 2025, Elsevier. (j) Proposed photocatalytic mechanism for Cu@PDI(30%)-NZU67. (k) Photocatalytic activity: Cu@PDI(30%)-NZU67 (50 mg), irradiation wavenumber = 420 nm, TEOA (0.3 M), and MeCN/deionized H_2O (4 : 1 v/v). (l) AQE results of Cu@PDI(30%)-NZU67. Reproduced from ref. 147. Copyright 2024, Elsevier.

fixation.[158] Furthermore, existing photocatalysts exhibit sluggish charge transfer kinetics, resulting in unsatisfactory N_2 fixation activity. Therefore, developing green and efficient ammonia synthesis technologies is essential for sustainable global development.

PDI represents a prototypical n-type organic semiconductor among diverse organic semiconductor materials, which is famous for its exceptional visible-light absorption capacity and robust chemical stability with great potential in photocatalytic N_2 fixation. In the study conducted by Yang and coworkers,[159] notably, the BOPDI photocatalyst achieved an NH_3 production rate of 74.0 μmol g^{-1} h^{-1} without sacrificial agents or cocatalysts, representing an 11-fold enhancement over conventional PDIs. The apparent quantum yield (AQY) for NH_3 generation

reached 1.29% under 450 nm monochromatic irradiation. Mechanistic studies attribute this performance to the intensified IEF, which directs electron migration toward embedded catalytic units while localizing photoinduced holes on benzene/perylene moieties (Fig. 17a–c). This spatial charge separation creates long-lived intermediate states: electrons activate N_2 to form NH_3, while holes drive H_2O oxidation to O_2. This work constitutes the first demonstration of PDI-based composites for photocatalytic N_2 fixation to ammonia. In another study, Wang et al.[160] established a facile solution-phase self-assembly strategy to generate IEFs in PDI-triazine-based polymers (Fig. 17d). The optimized PDIMA-2 photocatalyst achieves exceptional nitrogen fixation performance (49.90 μmol g^{-1} h^{-1}) without co-catalysts or sacrificial agents – surpassing pristine PDI by ~10-fold and outperforming carbon
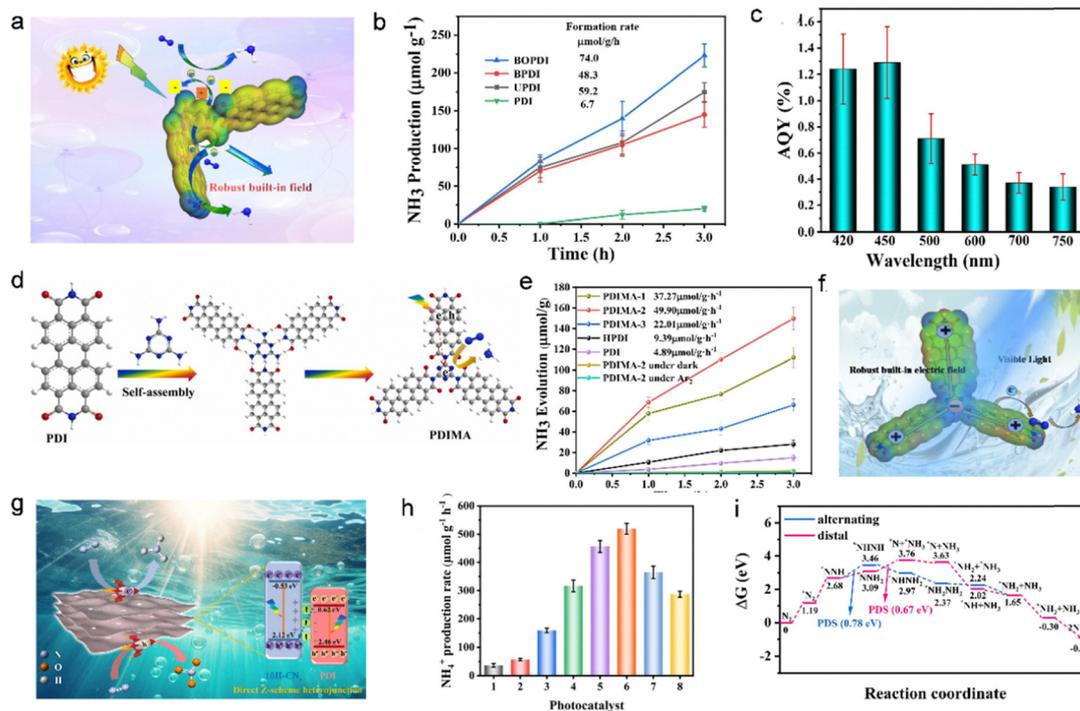
Fig. 17 (a) Plausible mechanism for the photocatalytic N$_2$ fixation over BOPDI under visible light irradiation. (b) NH$_3$ evolution rates over the as-prepared BOPDI catalysts. (c) Apparent quantum efficiency (AQY) of BOPDI. Reproduced from ref. 159. Copyright 2022, Elsevier. (d) Schematic diagram of the synthetic route. (e) Ammonia synthesis rates over different samples. (f) Diagram of the photocatalytic nitrogen fixation mechanism over PDIMA-2. Reproduced from ref. 160. Copyright 2022, Elsevier. (g) Direct Z-scheme heterojunction of 10H-CNv. (h) Average NH$_4^+$ yields for different photocatalysts. (i) Gibbs free energy diagrams of the photocatalytic reduction of ammonia by N$_2$ in 30% PDI/10H-CN$_v$ composites. Reproduced from ref. 161. Copyright 2024, Elsevier.

materials (Fig. 17e and f). Notably, significant NH$_3$ production persists under 750 nm monochromatic irradiation. Extended near-infrared absorption originates from triazine-PDI π–π stacking-induced LUMO–HOMO orbital overlap. Mechanistic studies reveal the IEF arises from face-to-face molecular dipoles and π-stacking arrangements, dramatically enhancing carrier separation/migration. Recently, Cui and his co-workers[161] constructed Z-scheme PDI/10H-CNv heterojunctions *via in situ* condensation (Fig. 17g). Nitrogen vacancies and curled pores in 10H-CNv boosted N$_2$ adsorption sites, while the enhanced IEF directed electron–hole separation. This synergy achieved 519.2 μmol g^{-1} h^{-1} NH$_3$ and 135.9 μmol g^{-1} h^{-1} (Fig. 17h and i).

4.4. Pollutant degradation

Photocatalysis represents a crucial, economical, and effective strategy for addressing environmental pollution.[162–164] Organic semiconductors serve as promising photocatalysts due to their facile synthesis, low cost, tunable functionalization, earth abundance, and robust photochemical stability. PDI, a conventional organic semiconductor widely used in dyes, solar cells, and optoelectronic devices, has recently gained significant attention for photocatalytic applications. In environmental remediation, PDI-based nanocomposites effectively degrade diverse aqueous organic pollutants including antibiotics and phenolic compounds (Table 3). Theoretical calculations reveal PDI's frontier molecular orbitals: LUMO and HOMO energies

derive from carbon and oxygen atomic orbitals, with nitrogen atoms acting as nodal points in π-orbital wavefunctions. Consequently, PDI's electronic structure primarily depends on π–π stacking interactions.[165] When a PDI-based photocatalyst is excited under illumination, photogenerated electrons in the CB reduce adsorbed O$_2$ to generate strongly oxidizing superoxide radicals ($^•$O$_2^-$). Simultaneously, VB holes migrate to the material surface, producing hydroxyl radicals ($^•$OH) and directly participating in oxidation. These reactive species ($^•$O$_2^-$, $^•$OH, and h$^+$) subsequently mineralize organic pollutants into nontoxic inorganic compounds and low-toxicity small molecules.

Antibiotics and pharmaceutical metabolites accumulating in aquatic environments represent persistent ecological threats due to structural complexity and degradation resistance.[166–169] Conventional water treatment technologies fail to ensure complete elimination. Heterojunction photocatalysts incorporating PDI offer transformative solutions through extended spectral utilization and enhanced carrier separation efficiency. Current advances include strategically designed type-II, Z-scheme, and S-scheme architectures *via* controlled integration of PDI with complementary semiconductors, such as g-C$_3$N$_4$, metal–organic frameworks, and metal oxides. These designs not only broaden the light absorption range, but also markedly enhance photocatalytic activity through interfacial charge transfer mechanisms. This section systematically reviews the latest advancements in PDI-based heterojunctions for the degradation of antibiotics and
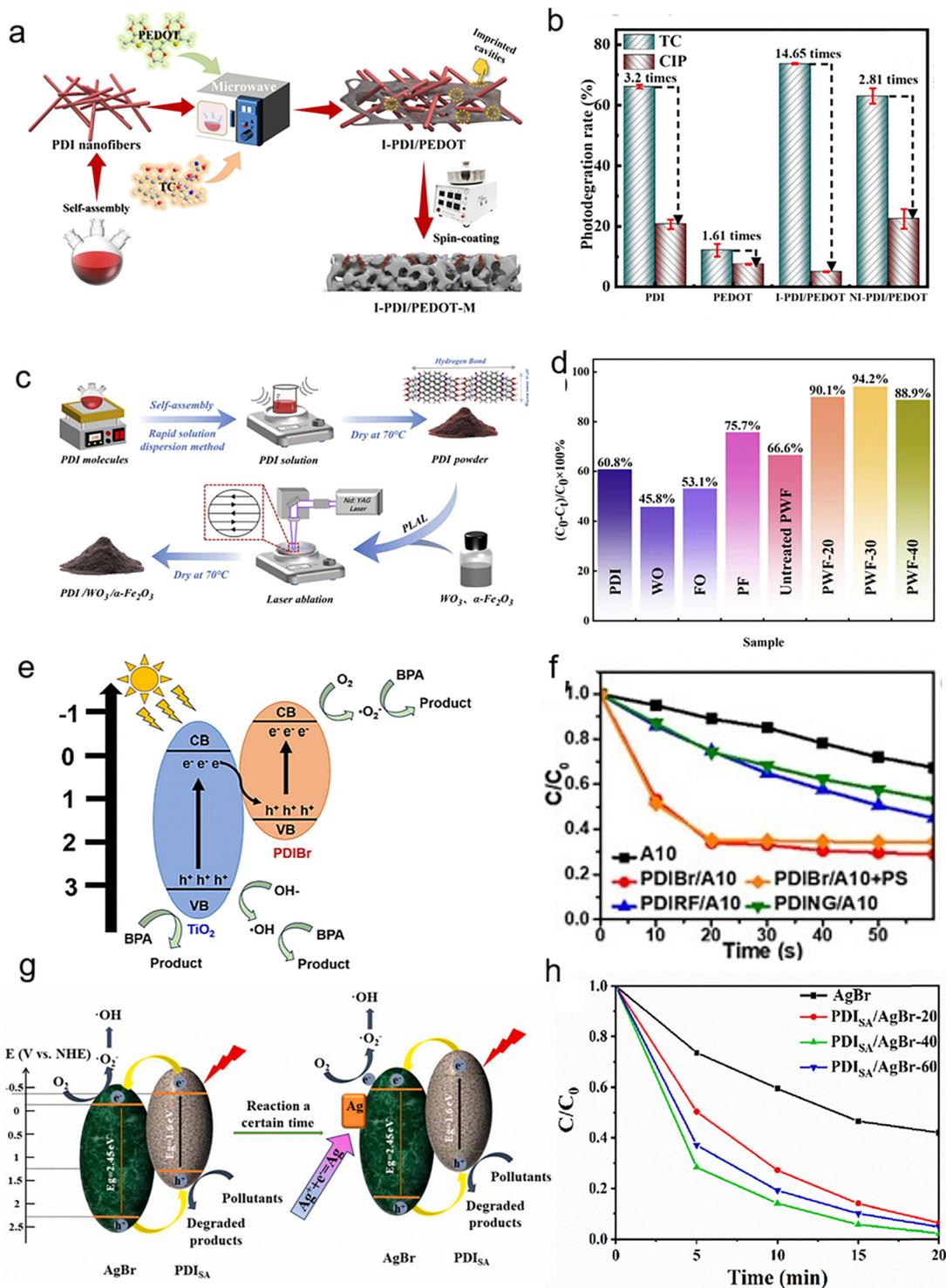
Fig. 18 (a) Synthesis process schematic of I-PDI/PEDOT-M. (b) The photodegradation rate of TC and CIP by different powder materials. Reproduced from ref. 170. Copyright 2023, Elsevier. (c) Flow chart of pulsed laser preparation of PDI/WO$_3$/α-Fe$_2$O$_3$ composites. (d) Total removal rate of TC in different samples. Reproduced from ref. 171. Copyright 2025, Elsevier. (e) Schematic illustrations of the PDIBr/A10 photocatalytic mechanism. (f) Photodegradation efficiency of A10 base composites about BPA. Reproduced from ref. 172. Copyright 2024, Elsevier. (g) Photocatalytic degradation mechanism of rhodamine B over PDI$_{SA}$/AgBr composite under visible light. (h) Degradation curves of RhB. Reproduced from ref. 175. Copyright 2024, Elsevier.

drug residues, elucidates the underlying mechanisms driving performance enhancement, and explores potential directions for future technological optimization.

For example, an imprinted PDI/PEDOT type-II heterojunction photocatalyst film (I-PDI/PEDOT-M) was engineered *via* *N*-methyl-pyrrolidone (NMP)-induced surface self-corrosion assisted rapid

spin-coating[170] (Fig. 18a). Under 1 h visible light irradiation, the degradation efficiencies for tetracycline (TC) and ciprofloxacin (CIP) reached 73.7% and 5.0% respectively. Notably, TC degradation efficiency exceeded CIP by 14.65-fold (Fig. 18b). This pronounced divergence originates from the type-II heterojunction between PDI and PEDOT, which enables directional carrier separation that sustains superior photocatalytic activity in I-PDI/PEDOT-M. Mao et al.[171] successfully synthesized a PDI/WO$_3$/α-Fe$_2$O$_3$, PWF composite photocatalyst with a dual Z-scheme heterojunction via the pulsed laser ablation in liquid (PLAL) technique (Fig. 18c). Photocatalytic performance evaluation revealed that the PWF composite achieved 94.2% TC removal efficiency under 180 min of irradiation using a 15 W low-pressure mercury lamp (λ = 254 nm) (Fig. 18d). The enhanced photocatalytic activity can be primarily attributed to two key factors: (1) dual mechanisms drive performance enhancement; (2) augmented adsorption capacity via site density/surface charge optimization; (3) band-engineered dual Z-scheme heterojunction enabling synergistic photoconversion-charge separation efficiency gains.

Besides antibiotics, PDI-based photocatalysts can also be employed for the degradation of phenols. In a related study, through solvent-exchange self-assembly, Zha et al.[172] constructed Z-scheme PDIBr/TiO$_2$(A10) heterojunctions. The composite demonstrated dual-mode BPA degradation: 71.04% (sacrificial-agent-free) vs. 71.7% (persulfate-assisted) under visible light (Fig. 18e). The composite demonstrated dual-mode BPA degradation of 71.04% (sacrificial-agent-free) vs. 71.7% (persulfate-assisted) under visible light (Fig. 18f). Critical enhancement derives from interfacial H-aggregates with π–π orbital overlap that enable directional charge transport and inhibit recombination. Spectroscopic evidence verifies the Z-scheme mechanism as the principal BPA degradation route.

In addition to phenols and antibiotics, PDI-based materials can also be used to degrade other pollutants, such as rhodamine b, methylene blue and methyl orange etc. Zhang et al.[173] successfully fabricated PDI/BiO$_2$-type-II heterojunctions through ultrasonic-assisted self-assembly technology. The materials exhibited remarkable photocatalytic performance under visible light irradiation, achieving a remarkable degradation efficiency. The key factor behind the enhanced performance was the IEF in type-II heterojunctions, which effectively drives the spatial separation of photogenerated carriers. Zhang et al.[174] achieved efficient synthesis of PDI/Bi$_2$O$_4$ type-II heterojunction photocatalysts using water bath heating coupled with ultrasonic dispersion. Remarkably, the 5% PDISA/Bi$_2$O$_4$ material degraded 98.6% of RhB and 97.0% of methylene blue within 25 min under visible light. The key mechanism involved an IEF formed at the heterojunction interface, which critically accelerated the separation and migration of photogenerated carriers, leading to superior photocatalytic performance. Furthermore, Xu et al.[175] fabricated PDISA/AgBr type-II organic–inorganic heterojunctions via chemical co-precipitation (Fig. 18g). Attributed to the synergistic effects of type-II heterojunctions – enhancing photogenerated carrier separation and broadening light absorption – the PDISA/AgBr-40 composite achieved 97.8% RhB degradation in 20 min under visible light (Fig. 18h).

5. Conclusions and outlook

This review comprehensively examines recent advancements in enhancing the photocatalytic performance of PDI-based composites through strategic structural engineering and functionalization. Following an analysis of the fundamental molecular architecture and electronic properties of PDI, we discuss several synthetic methods for fabricating PDI-based photocatalysts, correlating their physicochemical properties with performance metrics. Subsequently, we systematically evaluate the deployment of these materials across diverse photocatalytic applications, with particular emphasis on mechanistic insights governing charge transfer pathways. Due to their tunable band structures and exceptional photostability, PDI-based systems demonstrate significant promise in renewable energy conversion and environmental remediation. Notwithstanding these merits, persistent challenges in carrier recombination kinetics, scalability, and long-term stability necessitate still further investigation to realize their full technological potential. Specifically, as follows:

(1) PDI-based heterojunctions are predominantly assembled through electrostatic assembly, covalent/non-covalent conjugation, or semiconductor surface adsorption. Nevertheless, progressive disruption of interfacial chemical integrity during extended photocatalytic operation compromises charge transfer kinetics and catalytic efficacy. Strategic reinforcement of these interfaces through rational engineering constitutes an essential research priority to ensure operational longevity and practical deployment of PDI heterojunction systems.

(2) Further exploration of PDI's surface/structural properties is essential to optimize its optical and photocatalytic performance. Unique morphologies, exemplified by high-surface-area PDI nanosheets, offer advantages including large specific surface area, reduced charge recombination, and enhanced light utilization. While conventional nanostructures (nanosheets, nanowires, nanorods) are well-understood, high-performance configurations integrating elevated specific surface area with enhanced active site exposure – exemplified by quantum dots, hollow tubes, and hollow spheres – necessitate further exploration.

(3) Current PDI-based composites predominantly absorb visible light, while the near-infrared (NIR) region (43% of solar spectrum) remains underutilized. Substantial research efforts should therefore focus on developing advanced PDI photocatalysts capable of effective NIR light harvesting to enhance solar energy conversion efficiency.

(4) Advancing the rational design and functional efficacy of PDI-based photocatalysts necessitates a comprehensive mechanistic elucidation of their photocatalytic processes. Beyond fundamental charge carrier dynamics, rigorous investigation into the thermodynamics and microkinetics of surface-mediated catalytic reactions is imperative. State-of-the-art in situ spectroscopic characterization coupled with first-principles computational modelling provides indispensable tools for such fundamental inquiries. These methodologies will unravel critical structure–function relationships, ultimately enabling the precision engineering of PDI-based photocatalysts with exceptional quantum efficiency and reaction specificity.

(5) The established synthetic routes for PDI monomers and polymers remain procedurally intricate, cost-intensive, associated with environmental risks toxic modifiers/solvents, and poor reactor compatibility due to aggregation-induced clogging. To address these challenges, recent advances employ biocompatible functionalization and solvent-free synthesis to minimize toxicity precluding scalable industrial manufacturing and *e.g.*, 3D-printed monoliths to enhance dispersibility. These synergistic strategies achieve cost-effective, environmentally benign (OECD-compliant), and industrially adaptable PDI systems, demonstrating scalable potential for environmental remediation and energy conversion applications.

(6) Current research on PDI supramolecular photocatalysts remains predominantly confined to laboratory-scale investigations. Translational implementation for authentic environmental remediation scenarios merits prioritized exploration.

(7) The growing adoption of additive manufacturing in catalyst engineering enables precise reconfiguration of macroscopic architectures, offering unprecedented control over mass transport and light harvesting dynamics. Integrating 3D printing technologies with molecularly tailored PDI systems constitutes a promising frontier for designing spatially programmable photocatalysts – where supramolecular organization and reactor geometry synergistically optimize quantum efficiency and scalability.

The future development of PDI-based photocatalysis presents both transformative opportunities and critical challenges. This review establishes a framework for designing high-performance PDI systems, emphasizing four key metrics, *i.e.*, photocatalytic activity, structural stability, reaction selectivity, and visible-light harvesting capacity. Deeper integration of theoretical simulations with experimental validation will accelerate mechanistic understanding and material innovation. With sustained interdisciplinary efforts, PDI-based photocatalysts are poised to enable paradigm-shifting applications in sustainable chemistry.

Author contributions

Initiation and conceptualization: G. L. and P. W. Methodology and formal analysis: Y. X., Z. C., and X. L. Investigation: Y. X., G. D., X. W., and Z. W. Funding acquisition: G. L. Project administration: G. L. Supervision: G. L., and P. W. Writing – original draft: Y. X., Z. C., and X. L. Writing – review and editing: G. L. and P. W.

Conflicts of interest

The authors declare that they have no competing interests.

Data availability

No primary research results, software or code have been included and no new data were generated or analysed as part of this review.

Acknowledgements

References

1 J. Zhang, D. Yan, G. Ding, X. Wang, C. Li, S. Zhong, Y. Yu, L. Shuai and G. Liao, *Angew. Chem., Int. Ed.*, 2025, e202511448, DOI: **10.1002/anie.202511448**.

2 G. Liao, E. Sun, E. B. G. Kana, H. Huang, I. A. Sanusi, P. Qu, H. Jin, J. Liu and L. Shuai, *Carbohydr. Polym.*, 2024, **341**, 122351.

3 G. Ding, J. Zhang, D. Yan, Y. Yu, L. Shuai, L. Chen and G. Liao, *Nano Lett.*, 2025, **25**, 8984–8992.

4 J. Zhang, Y. Yang, G. Ding, Z. Wang, P. Wang, C. Li and G. Liao, *Chem. Eng. J.*, 2025, **505**, 159165.

5 S. Liu, Y. Guo, S. Yi, S. Yan, C. Ouyang, F. Deng, C. Li, G. Liao and Q. Li, *Sep. Purif. Technol.*, 2023, **307**, 122727.

6 J. Fang, M. Chen, X. Wang, Z. Huang, S. Zhao, P. Wang, Q. Li and G. Liao, *Chem. Eng. J.*, 2025, **516**, 164208.

7 C. Li, G. Ding, P. Wang, K. Liu, B. Yang and G. Liao, *Dalton Trans.*, 2025, **54**, 889–897.

8 Y. Liu, S. Huang, X. Huang and D. Ma, *Mater. Horiz.*, 2024, **11**, 1611–1637.

9 Y. Ahmed, K. R. Dutta, P. Akhtar, M. A. Hossen, M. J. Alam, O. A. Alharbi, H. AlMohamadi and A. W. Mohammad, *Beilstein J. Nanotechnol.*, 2025, **16**, 264–285.

10 C. Li, H. Lu, G. Ding, Q. Li and G. Liao, *Catal. Sci. Technol.*, 2023, **13**, 2877–2898.

11 Z. Wang, G. Ding, J. Zhang, X. Lv, P. Wang, L. Shuai, C. Li, Y. Ni and G. Liao, *Chem. Commun.*, 2024, **60**, 204–207.

12 M. Devaraj and X. Zhou, *Coord. Chem. Rev.*, 2025, **532**, 216509.

13 G. Liao, Y. He, H. Wang, B. Fang, N. Tsubaki and C. Li, *Device*, 2023, **1**, 100173.

14 C. Li, B. Cheng, H. Lu, G. Ding, Z. Jiang and G. Liao, *Inorg. Chem.*, 2023, **62**, 6843–6850.

15 G. Liao and M. Wu, *Innovation Energy*, 2024, **1**, 100047.

16 M. Faraji, M. Yousefi, S. Yousefzadeh, M. Zirak, N. Naseri, T. H. Jeon, W. Choi and A. Z. Moshfegh, *Energy Environ. Sci.*, 2019, **12**, 59–95.

17 T. Luo, L. Gilmanova and S. Kaskel, *Coord. Chem. Rev.*, 2023, **490**, 215210.

18 C. Li, N.-Y. Huang, Y. Yang, Q. Xu and G. Liao, *Coord. Chem. Rev.*, 2025, **524**, 216292.

19 W. Zhang, C. Shu, H. Cui, Q. Wan, C.-T. Au, B. Yi and H. Yang, *Macromol. Rapid Commun.*, 2023, **44**, 2300012.

20 Y. Guo, B. Liu, J. Zhang, G. Wang, C. Pan, H. Zhao, C. Wang, F. Yu, Y. Dong and Y. Zhu, *Appl. Catal., B*, 2024, **340**, 123217.

21 W. Che, C. Sun, Z. Wu, Y. Sun and Q. Shang, *J. Cleaner Prod.*, 2024, **453**, 142235.

22 V. Adepu, M. Tathacharya, R. S. Fernandes, A. Tiwari, S. Siraj, S. Kanungo, N. Dey and P. Sahatiya, *Adv. Mater. Technol.*, 2023, **8**, 2201633.

23 N. Fabre, T. Fukaminato, I. Ikariko, L. Chocron, A. Brosseau and R. Métivier, *Adv. Opt. Mater.*, 2024, **12**, 2400452.

24 Y. Ma, C. Hao, Z. Ning, F. Zhang, J. Cui, T. Jiang and Z. Shi, *Inorg. Chem. Commun.*, 2024, **166**, 112694.

25 Y. H. Koo, Y. Tsutsui, M. Omoto, Y. Yomogida, K. Yanagi, Y. K. Kato, M. A. Hermosilla-Palacios, J. L. Blackburn and S. Seki, *J. Phys. Chem. Lett.*, 2025, **16**, 3232–3239.

26 D. Powell and L. Whittaker-Brooks, *Mater. Horiz.*, 2022, **9**, 2026–2052.

27 F. Brust, O. Nagler, K. Shoyama, M. Stolte and F. Würthner, *Adv. Opt. Mater.*, 2023, **11**, 2202676.

28 R. Gerdes, D. Wöhrle, W. Spiller, G. Schneider, G. Schnurpfeil and G. Schulz-Ekloff, *J. Photochem. Photobiol. A: Chem.*, 1997, **111**, 65–74.

29 Y. Xiao, G. Ding, J. Tao, Z. Wang, Z. Chen, L. Chen, L. Shuai and G. Liao, *Nat. Commun.*, 2025, **16**, 7476.

30 H. Li, C. Wang, X. Bai, X. Wang, B. Sun, D. Li, L. Zhao, R. Zong and D. Hao, *Mater. Chem. Front.*, 2020, **4**, 2673–2687.

31 Q. Zhang, L. Jiang, J. Wang, Y. Zhu, Y. Pu and W. Dai, *Appl. Catal., B*, 2020, **277**, 119122.

32 B. Yang, L. Lu, S. Liu, W. Cheng, H. Liu, C. Huang, X. Meng, R. D. Rodriguez and X. Jia, *J. Mater. Chem. A*, 2024, **12**, 3807–3843.

33 Y. Sun, D. Wang and Y. Zhu, *Chem. Eng. J.*, 2022, **438**, 135667.

34 Z. Wang, Q. Peng, X. Huang, Q. Ma, J. Shao and Q. Shen, *Dyes Pigments*, 2021, **185**, 108877.

35 J. Tan, G. Zhang, C. Ge, J. Liu, L. Zhou, C. Liu, X. Gao, A. Narita, Y. Zou and Y. Hu, *Org. Lett.*, 2022, **24**, 2414–2419.

36 S. Chen, P. Slattum, C. Wang and L. Zang, *Chem. Rev.*, 2015, **115**, 11967–11998.

37 C. Huang, S. Barlow and S. R. Marder, *J. Org. Chem.*, 2011, **76**, 2386–2407.

38 D. Liu, J. Wang, X. Bai, R. Zong and Y. Zhu, *Adv. Mater.*, 2016, **28**, 7284–7290.

39 J. Wang, W. Shi, D. Liu, Z. Zhang, Y. Zhu and D. Wang, *Appl. Catal., B*, 2017, **202**, 289–297.

40 F. Würthner, C. R. Saha-Möller, B. Fimmel, S. Ogi, P. Leowanawat and D. Schmidt, *Chem. Rev.*, 2016, **116**, 962–1052.

41 J. Wang, D. Liu, Y. Zhu, S. Zhou and S. Guan, *Appl. Catal., B*, 2018, **231**, 251–261.

42 M. Más-Montoya and R. A. J. Janssen, *Adv. Funct. Mater.*, 2017, **27**, 1605779.

43 B. Wei, H. Li, H. Chu, H. Dong, Y. Zhang, C.-L. Sun and Y. Li, *Langmuir*, 2024, **40**, 6493–6505.

44 H. Wu, L. Xue, Y. Shi, Y. Chen and X. Li, *Langmuir*, 2011, **27**, 3074–3082.

45 Y. Xu, X. Zhu, H. Yan, P. Wang, M. Song, C. Ma, Z. Chen, J. Chu, X. Liu and Z. Lu, *Chin. J. Catal.*, 2022, **43**, 1111–1122.

46 X. Yang, S. Zhang, P. Li, S. Gao and R. Cao, *J. Mater. Chem. A*, 2020, **8**, 20897–20924.

47 H. Langhals, S. Demmig and T. Potrawa, *J. Prakt. Chem.*, 1991, **333**, 733–748.

48 S. Tatemichi, M. Ichikawa, T. Koyama and Y. Taniguchi, *Appl. Phys. Lett.*, 2006, **89**, 112108.

49 Y. Liu, M. D. Cole, Y. Jiang, P. Y. Kim, D. Nordlund, T. Emrick and T. P. Russell, *Adv. Mater.*, 2018, **30**, 1705976.

50 Y.-J. Kim, Y. Lee, K. Park, C. W. Ahn, H.-T. Jung and H.-J. Jeon, *J. Phys. Chem. Lett.*, 2020, **11**, 3934–3940.

51 R. Guan, X. Cheng, Y. Chen, Z. Wu, Z. Zhao, Q. Shang, Y. Sun and Z. Sun, *Nano Res.*, 2023, **16**, 10770–10778.

52 S. Ghosh, X.-Q. Li, V. Stepanenko and F. Würthner, *Chem. – Eur. J.*, 2008, **14**, 11343–11357.

53 M. E. Ozser, *Mater. Today Commun.*, 2021, **27**, 102446.

54 S. Izawa, K. Uchida, M. Nakamura, K. Fujimoto, J. Roudin, J.-H. Lee, T. Inuzuka, T. Nakamura, M. Sakamoto, Y. Nakayama, M. Hiramoto and M. Takahashi, *Chem. – Eur. J.*, 2021, **27**, 14081–14091.

55 Z. Li, J. Jiao, W. Fu, K. Gao, X. Peng, Z. Wang, H. Zhuo, C. Yang, M. Yang, G. Chang, L. Yang, X. Zheng, Y. Yan, F. Chen, M. Zhang, Z. Meng and X. Shang, *Angew. Chem., Int. Ed.*, 2024, **63**, e202412977.

56 W. Liu, C. He, S. Huang, K. Zhang, W. Zhu, L. Liu, Z. Zhang, E. Zhu, Y. Chen, C. Chen and Y. Zhu, *Angew. Chem., Int. Ed.*, 2023, **62**, e202304773.

57 Y. Pu, F. Bao, D. Wang, X. Zhang, Z. Guo, X. Chen, Y. Wei, J. Wang and Q. Zhang, *J. Environ. Chem. Eng.*, 2022, **10**, 107123.

58 R. Yan, M. Song, P. Chen, H. Song, C. Fu, H. Peng and S.-F. Yin, *J. Colloid Interface Sci.*, 2023, **651**, 68–75.

59 L. Zeng, T. Liu, C. He, D. Shi, F. Zhang and C. Duan, *J. Am. Chem. Soc.*, 2016, **138**, 3958–3961.

60 X. Gao, K. Gao, X. Li, Y. Shang and F. Fu, *Catal. Sci. Technol.*, 2020, **10**, 372–381.

61 Y. Guo, B. Liu, J. Zhang, C. Wang, G. Wang, C. Pan, H. Zhao, Y. Dong and Y. Zhu, *Appl. Catal., B*, 2024, **350**, 123915.

62 K. Kong, S. Zhang, Y. Chu, Y. Hu, F. Yu, H. Ye, H. Ding and J. Hua, *Chem. Commun.*, 2019, **55**, 8090–8093.

63 T. Weil, T. Vosch, J. Hofkens, K. Peneva and K. Müllen, *Angew. Chem., Int. Ed.*, 2010, **49**, 9068–9093.

64 T. T. Clikeman, E. V. Bukovsky, X.-B. Wang, Y.-S. Chen, G. Rumbles, S. H. Strauss and O. V. Boltalina, *Eur. J. Org. Chem.*, 2015, 6641–6654.

65 F. Zhang, Y. Ma, Y. Chi, H. Yu, Y. Li, T. Jiang, X. Wei and J. Shi, *Sci. Rep.*, 2018, **8**, 8208.

66 B. Zhang, S. Wang, S. Min, K. Li, L. Kang and W. Lin, *Mol. Catal.*, 2024, **560**, 114116.

67 M.-H. Lin, M.-H. Fang, Q. Liao and M.-J. Lin, *Dyes Pigments*, 2023, **220**, 111730.

68 Y. Zhang, D. Wang, W. Liu, Y. Lou, Y. Zhang, Y. Dong, J. Xu, C. Pan and Y. Zhu, *Appl. Catal., B*, 2022, **300**, 120762.

69 Y. Sheng, W. Li, Y. Zhu and L. Zhang, *Appl. Catal., B*, 2021, **298**, 120585.

70 M. Gryszel, T. Schlossarek, F. Würthner, M. Natali and E. D. Głowacki, *ChemPhotoChem*, 2023, **7**, e202300070.

71 Z. Zhang, X. Chen, H. Zhang, W. Liu, W. Zhu and Y. Zhu, *Adv. Mater.*, 2020, **32**, 1907746.

72 A. Cao, R. Li, X. Xu, W. Huang, Y. He, J. Li, M. Sun, X. Chen and L. Kang, *Appl. Catal., B*, 2022, **309**, 121293.

73 X. Wu, B. Hu, D. Li, B. Chen, Y. Huang, Z. Xie, L. Li, N. Shen, F. Yang, W. Shi, M. Chen and Y. Zhu, *Angew. Chem., Int. Ed.*, 2023, **62**, e202313787.

74 S. Huang, H. Zhang, W. Li, L. Liu, J. Xu, M. Chong, J. Li and Y. Zhu, *Appl. Catal., B*, 2024, **347**, 123790.

75 C. Huang, W. Yu, N. Fang, C. He, Y. Chu and B. Lai, *Sep. Purif. Technol.*, 2025, **360**, 131146.

76 Y.-J. Chen, J.-Z. Zhang, Z.-X. Wu, Y.-X. Qiao, L. Zheng, F. Wondu Dagnaw, Q.-X. Tong and J.-X. Jian, *Angew. Chem., Int. Ed.*, 2024, **63**, e202318224.

77 D. Liu, X. Yang, P. Chen, X. Zhang, G. Chen, Q. Guo, H. Hou and Y. Li, *Adv. Mater.*, 2023, **35**, 2300655.

78 L. Yang, Y. Fu, F. Sun, M. Deng, C. Zhang, N. Li, D. Hao, Q. Wang and G. Zhuang, *J. Colloid Interface Sci.*, 2023, **639**, 472–483.

79 H. Wang, L. Zhang, Z. Chen, J. Hu, S. Li, Z. Wang, J. Liu and X. Wang, *Chem. Soc. Rev.*, 2014, **43**, 5234–5244.

80 Y.-P. Yuan, L.-W. Ruan, J. Barber, S. C. Joachim Loo and C. Xue, *Energy Environ. Sci.*, 2014, **7**, 3934–3951.

81 S. J. A. Moniz, S. A. Shevlin, D. J. Martin, Z.-X. Guo and J. Tang, *Energy Environ. Sci.*, 2015, **8**, 731–759.

82 K. Zhang, J. Wang, W. Jiang, W. Yao, H. Yang and Y. Zhu, *Appl. Catal., B*, 2018, **232**, 175–181.

83 Y. Li, Y. Fang, Z. Cao, N. Li, D. Chen, Q. Xu and J. Lu, *Appl. Catal., B*, 2019, **250**, 150–162.

84 H. Wang, Y. Zhou, J. Wang, A. Li and P. François-Xavier Corvini, *Chem. Eng. J.*, 2022, **433**, 133622.

85 M. Wu, H. Yang, Q. Wu, Z. He and S. Wang, *J. Environ. Chem. Eng.*, 2024, **12**, 112246.

86 G. Liao, C. Li, X. Li and B. Fang, *Cell Rep. Phys. Sci.*, 2021, **2**, 100355.

87 H. Zhu, C. Zhang, K. Xie, X. Li and G. Liao, *Chem. Eng. J.*, 2023, **453**, 139775.

88 C. D. Jaeger and A. J. Bard, *J. Phys. Chem.*, 1979, **83**, 3146–3152.

89 H. Tada, T. Mitsui, T. Kiyonaga, T. Akita and K. Tanaka, *Nat. Mater.*, 2006, **5**, 782–786.

90 Q. Huang, Q. Zhang, S. Yuan, Y. Zhang and M. Zhang, *Appl. Surf. Sci.*, 2015, **353**, 949–957.

91 J. Yu, S. Wang, J. Low and W. Xiao, *Phys. Chem. Chem. Phys.*, 2013, **15**, 16883–16890.

92 Y. Yuan, R.-T. Guo, L.-F. Hong, X.-Y. Ji, Z.-D. Lin, Z.-S. Li and W.-G. Pan, *Mater. Today Energy*, 2021, **21**, 100829.

93 P. Zhou, J. Yu and M. Jaroniec, *Adv. Mater.*, 2014, **26**, 4920–4935.

94 G. Zhang, Z. Wang and J. Wu, *Nanoscale*, 2021, **13**, 4359–4389.

95 X. Xu, L. Meng, J. Zhang, S. Yang, C. Sun, H. Li, J. Li and Y. Zhu, *Angew. Chem., Int. Ed.*, 2024, **63**, e202308597.

96 W. Dai, L. Jiang, J. Wang, Y. Pu, Y. Zhu, Y. Wang and B. Xiao, *Chem. Eng. J.*, 2020, **397**, 125476.

97 K. Shi, M. Zhou, F. Wang, X. Li, W. Huang, K. Lu, K. Yang and C. Yu, *Chemosphere*, 2023, **329**, 138617.

98 C. Li, B. Cheng, J. Shen, H. Wang, M. Yi, P. Gu, R. Liu, G. Liao and Z. Jiang, *Sep. Purif. Technol.*, 2025, **360**, 131116.

99 S. Liu, Y. Zhang, Y. Guo, Z. Cheng, M. Yuan, Z. Xu, G. Liao and Q. Li, *J. Colloid Interface Sci.*, 2025, **686**, 45–62.

100 C. Li, H. Lu, G. Ding, T. Ma, S. Liu, L. Zhang and G. Liao, *Chin. J. Catal.*, 2024, **65**, 174–184.

101 J. Low, J. Yu, M. Jaroniec, S. Wageh and A. A. Al-Ghamdi, *Adv. Mater.*, 2017, **29**, 1601694.

102 J. Wei, G. Zhang, S. Xie, Z. Zhang, T. Gao, M. Zhang and X. Li, *Angew. Chem., Int. Ed.*, 2025, **64**, e202500441.

103 F. Wu, Y. Tang, Y. Pan, J. Han, W. Xing, J. Zhang, G. Wu and Y. Huang, *Small*, 2025, 2500670, DOI: **10.1002/smll.202500670**.

104 J. Yang, H. Miao, W. Li, H. Li and Y. Zhu, *J. Mater. Chem. A*, 2019, **7**, 6482–6490.

105 R. Chen, H. Lou, Y. Pang, D. Yang and X. Qiu, *Small*, 2024, **20**, 2306354.

106 N. Li, Y. Niu, W. An, F. Ruan, H. Wu, B. Hui, Y. Wang and G. Fan, *Appl. Catal., B*, 2025, **369**, 125141.

107 F. Zhang, H. Peng, S. Jiang, C. Wang, X. Xu and L. Wang, *Environ. Sci. Poll. Res.*, 2019, **26**, 8226–8236.

108 S. Linic, P. Christopher and D. B. Ingram, *Nat. Mater.*, 2011, **10**, 911–921.

109 H. Miao, J. Yang, Y. Wei, W. Li and Y. Zhu, *Appl. Catal., B*, 2018, **239**, 61–67.

110 D. Liu, L. Chen, W. Chen, M. Qin and S. Wei, *Dalton Trans.*, 2021, **50**, 4008–4016.

111 B. Yang, L. Lu, Q. Zhang, G. Ding, G. Liao, M. Zhang, X. Liu, R. D. Rodriguez and X. Jia, *Chem. Eng. J.*, 2025, **509**, 161236.

112 C. Li, X. Liu, G. Ding, P. Huo, Y. Yan, Y. Yan and G. Liao, *Inorg. Chem.*, 2022, **61**, 4681–4689.

113 Y. Liang, W. Gui, Z. Yang, K. Cheng, X. Zhou, C. Yang, J. Xu and W. Zhou, *RSC Adv.*, 2023, **13**, 11938–11947.

114 B. Palas and G. Ersöz, *J. Mol. Liq.*, 2024, **394**, 123717.

115 Y. Wang, H. Xu and X. Zhang, *Adv. Mater.*, 2009, **21**, 2849–2864.

116 W. Dai, L. Jiang, J. Wang, Y. Pu, Y. Zhu, Y. Wang and B. Xiao, *Chem. Eng. J.*, 2020, **397**, 125476.

117 H. Zhu, L. Gou, C. Li, X. Fu, Y. Weng, L. Chen, B. Fang, L. Shuai and G. Liao, *Device*, 2024, **2**, 100283.

118 C. Li, X. Liu, P. Huo, Y. Yan, G. Liao, G. Ding and C. Liu, *Small*, 2021, **17**, 2102539.

119 Y.-J. Zhang, J.-Z. Cheng, Y.-Q. Xing, Z.-R. Tan, G. Liao and S.-Y. Liu, *Mater. Sci. Semicond. Proc.*, 2023, **161**, 107463.

120 A. Muzammil, R. Haider, W. Wei, Y. Wan, M. Ishaq, M. Zahid, W. Yaseen and X. Yuan, *Mater. Horiz.*, 2023, **10**, 2764–2799.

121 G. Liao, X. Tao and B. Fang, *Matter*, 2022, **5**, 377–379.

122 G. Liao, Y. Gong, L. Zhang, H. Gao, G.-J. Yang and B. Fang, *Energy Environ. Sci.*, 2019, **12**, 2080–2147.

123 P. Chen, L. Blaney, G. Cagnetta, J. Huang, B. Wang, Y. Wang, S. Deng and G. Yu, *Environ. Sci. Technol.*, 2019, **53**, 1564–1575.

124 T. Sun, J. Song, J. Jia, X. Li and X. Sun, *Nano Energy*, 2016, **26**, 83–89.

125 H. Ding, Z. Wang, K. Kong, S. Feng, L. Xu, H. Ye, W. Wu, X. Gong and J. Hua, *J. Mater. Chem. A*, 2021, **9**, 7675–7683.

126 J. Yang, J. Jing, W. Li and Y. Zhu, *Adv. Sci.*, 2022, **9**, 2201134.

127 H. Xu, Z. Wang, S. Feng, X. Liu, X. Gong and J. Hua, *Int. J. Hydrogen Energy*, 2023, **48**, 8071–8081.

128 W. Yu, N. Fang, Z. Liu, Y. Chu and B. Lai, *Small*, 2024, **20**, 2407104.

129 Z. Chen, D. Yan, X. Wang, G. Ding, Z. Wang, Y. Xiao, X. Liu, P. Wang, L. Chen, L. Shuai and G. Liao, *ACS Catal.*, 2025, **15**, 13568–13580.

130 J. Li, J. Fang, H. Liang, Z. Wei, J. Fang, L. Qiu, X. Lu, F. Yang and G. Zeng, *Chem. Eng. J.*, 2025, 164628.

131 S. Peng, R. Wang, Y. Yang, S. Wang, E. Liang, B. Han, J. Li, X. Yu and Q. Zhang, *Macromol. Rapid Commun.*, 2025, **46**, 2400967.

132 Y. Sheng, W. Li, L. Xu and Y. Zhu, *Adv. Mater.*, 2022, **34**, 2102354.

133 W. Li, Z. Wei, Y. Sheng, J. Xu, Y. Ren, J. Jing, J. Yang, J. Li and Y. Zhu, *ACS Energy Lett.*, 2023, **8**, 2652–2660.

134 G. Ding, C. Li, L. Chen and G. Liao, *Energy Environ. Sci.*, 2024, **17**, 5311–5335.

135 G. Liao, G. Ding, B. Yang and C. Li, *Precis. Chem.*, 2024, **2**, 49–56.

136 K. Liu, M. A. Nawaz and G. Liao, *Coord. Chem. Rev.*, 2025, **535**, 216611.

137 G. Ding, C. Li, Y. Ni, L. Chen, L. Shuai and G. Liao, *EES Catal.*, 2023, **1**, 369–391.

138 Z. Chen, G. Ding, Z. Wang, Y. Xiao, X. Liu, L. Chen, C. Li, H. Huang and G. Liao, *Adv. Funct. Mater.*, 2025, **35**, 2423213.

139 F. Tian, X. Wu, J. Chen, X. Sun, X. Yan and G. Liao, *Dalton Trans.*, 2023, **52**, 11934–11940.

140 K. Liu, Y. Liao, P. Wang, X. Fang, J. Zhu, G. Liao and X. Xu, *Nanoscale*, 2024, **16**, 11096–11108.

141 Z. Zhao, F. Niu, P. Li, H. Wang, Z. Zhang, G. J. Meyer and K. Hu, *J. Am. Chem. Soc.*, 2022, **144**, 7043–7047.

142 W. Wu, H. Bi, Z. Zhang, L. Sun, R. Wei, L. Gao, X. Pan, J. Zhang and G. Xiao, *Colloids Surf. A*, 2023, **657**, 130486.

143 R. Yang, Q. Li, Z. Ma, S. Liu, D. Tian, D. Li and D. Jiang, *Chem. Eng. J.*, 2025, **506**, 160043.

144 R. Dalapati, M. Hunter, M. Sk, X. Yang and L. Zang, *ACS Appl. Mater. Interfaces*, 2024, **16**, 32344–32356.

145 S. Zheng, H. Du, L. Yang, M. Tan, N. Li, Y. Fu, D. Hao and Q. Wang, *J. Hazard. Mater.*, 2023, **447**, 130849.

146 Y. Li, Y.-H. Li, P. Wang, C. Zhao, C.-Y. Tang, S.-J. Gao and C.-C. Wang, *J. Environ. Chem. Eng.*, 2023, **11**, 109205.

147 F. M. A. Altalbawy, P. Sharma, F. H. Alsultany, A. Kumar, K. P. Vinay, I. S. Alalaq, M. Chahar, U. S. Altimari, A. M. Jabbar, M. M. Alam and L. H. Alzubaidi, *J. Mol. Struct.*, 2025, **1326**, 141088.

148 C. Zhu, C. Gong, D. Cao, L.-L. Ma, D. Liu, L. Zhang, Y. Li, Y. Peng and G. Yuan, *Angew. Chem., Int. Ed.*, 2025, **64**, e202504348.

149 M. Philippi, K. Kitzinger, J. S. Berg, B. Tschitschko, A. T. Kidane, S. Littmann, H. K. Marchant, N. Storelli, L. H. E. Winkel, C. J. Schubert, W. Mohr and M. M. M. Kuypers, *Nat. Commun.*, 2021, **12**, 4774.

150 S. Zhang, Y. Zhao, R. Shi, C. Zhou, G. I. N. Waterhouse, Z. Wang, Y. Weng and T. Zhang, *Angew. Chem., Int. Ed.*, 2021, **60**, 2554–2560.

151 Z. Lu, J. Zhang, Y. Wang, Y. Yu and L. Kong, *Mater. Horiz.*, 2025, **12**, 3286–3300.

152 M. Sharma, A. Kumar, D. Sajwan, K. Kumari, B. P. Mishra and V. Krishnan, *Adv. Sustainable Syst.*, 2025, **9**, 2400903.

153 J. S. Anderson, J. Rittle and J. C. Peters, *Nature*, 2013, **501**, 84–87.

154 G. Liao, C. Li, S.-Y. Liu, B. Fang and H. Yang, *Phys. Rep.*, 2022, **983**, 1–41.

155 G. Liao, C. Li, S.-Y. Liu, B. Fang and H. Yang, *Trends Chem.*, 2022, **4**, 111–127.

156 Q. Dong, X. Li, Y. Duan, X. He, X. Liang, F. Yu and C. Wang, *Appl. Catal., B*, 2025, **366**, 125042.

157 D. Zhu, L. Zhang, R. E. Ruther and R. J. Hamers, *Nat. Mater.*, 2013, **12**, 836–841.

158 Q. Li, D. Shen, Z. Xiao, X. Liu, X. Xu, M. Wu, W. Wang, L. Liu, Q. Li and X. Li, *Small*, 2025, **21**, 2411665.

159 S. Yang, X. Deng, P. Chen, G. Li, Q. Wang, Q. Wang and S.-F. Yin, *Chem. Eng. J.*, 2022, **441**, 136084.

160 Q. Wang, J. Cao, P. Chen, S. Yang, C. Fu, F. Liu and S.-F. Yin, *Appl. Catal., A*, 2023, **649**, 118978.

161 D. Cui, X. Yang, Y. Liu, M. Li, C. Wang and F. Li, *Sep. Purif. Technol.*, 2025, **356**, 130035.

162 Y. Qiao, C. Sun, J. Jian, T. Zhou, X. Xue, J. Shi, G. Che and G. Liao, *J. Mol. Liquids*, 2023, **385**, 122383.

163 G. Ding, Z. Wang, J. Zhang, P. Wang, L. Chen and G. Liao, *EcoEnergy*, 2024, **2**, 22–44.

164 C. Du, J. Xu, G. Ding, D. He, H. Zhang, W. Qiu, C. Li and G. Liao, *Nanomaterials*, 2023, **13**, 3066.

165 W. Zhou, G. Liu, B. Yang, Q. Ji, W. Xiang, H. He, Z. Xu, C. Qi, S. Li, S. Yang and C. Xu, *Sci. Total Environ.*, 2021, **780**, 146483.

166 Q. Wu, J. Wang, Z. Wang, Y. Xu, Z. Xing, X. Zhang, Y. Guan, G. Liao and X. Li, *J. Mater. Chem. A*, 2020, **8**, 13685–13693.

167 S. Liu, F. Deng, Y. Guo, C. Ouyang, S. Yi, C. Li, G. Liao and Q. Li, *ACS Appl. Nano Mater.*, 2024, **7**, 889–903.

168 G. Liao, Y. Gong, L. Zhong, J. Fang, L. Zhang, Z. Xu, H. Gao and B. Fang, *Nano Res.*, 2019, **12**, 2407–2436.

169 G. Liao, J. Fang, Q. Li, S. Li, Z. Xu and B. Fang, *Nanoscale*, 2019, **11**, 7062–7096.

170 Z. Lu, B. Li, B. Wei, G. Zhou, Y. Xu, J. Zhang, H. Chen, S. Hua, C. Wu and X. Liu, *Sep. Purif. Technol.*, 2023, **314**, 123609.

171 Z. Mao, P. Luo, J. Ling, X. Zhu, K. Sun, Y. Cao, D. Zhu and W. Liu, *J. Alloys Compd.*, 2025, **1011**, 178195.

172 K. Zha, L. Li, J. Zhang, S. Tang, X. Li, J. Hai, D. Fan, M. Li, Y. Liu and Z. Lu, *J. Photochem. Photobiol. A*, 2024, **451**, 115517.

173 X. Zhang, L. Shi and Y. Zhang, *J. Taiwan Inst. Chem. Eng.*, 2022, **132**, 104111.

174 X. Zhang, L. Shi, L. Yao and L. Cui, *Mater. Res. Bull.*, 2022, **146**, 111589.

175 T. Xu, S. Zhang, W. Zhang and L. Shi, *Opt. Mater.*, 2024, **147**, 114656.

176 H. Miao, J. Yang, Y. Sheng, W. Li and Y. Zhu, *Solar RRL*, 2021, **5**, 2000453.

177 Z. Liang, R. Shen, P. Zhang, Y. Li, N. Li and X. Li, *Chin. J. Catal.*, 2022, **43**, 2581–2591.

178 J. Yang, H. Miao, J. Jing, Y. Zhu and W. Choi, *Appl. Catal., B*, 2021, **281**, 119547.

179 C. Ye, J.-X. Li, H.-L. Wu, X.-B. Li, B. Chen, C.-H. Tung and L.-Z. Wu, *ACS Appl. Mater. Interfaces*, 2018, **10**, 3515–3521.

180 L. Liu, J. Liu, S. Zong, Z. Huang, X. Feng, J. Zheng and Y. Fang, *Int. J. Hydrogen Energy*, 2022, **47**, 39486–39498.

181 S. Chen, C. Wang, B. R. Bunes, Y. Li, C. Wang and L. Zang, *Appl. Catal., A*, 2015, **498**, 63–68.

182 X. Li, X. Lv, Q. Zhang, B. Huang, P. Wang, X. Qin, X. Zhang and Y. Dai, *J. Colloid Interface Sci.*, 2018, **525**, 136–142.

183 J. Chen, W. Lin, J. Lin and Y. Wang, *J. Mater. Chem. A*, 2025, **13**, 1095–1101.

184 X. Ji, X. Liu, Y. Guo and J. Zhang, *Chem. Eng. J.*, 2021, **425**, 131260.

185 H. Zhuang, F. Wang, K. Shi and K. Yang, *Catalysts*, 2023, **13**, 688.

186 Y. Jia, L. Duan, H. Li, C. Zhang, Q. Gao, H. Zhang, S. Li and M. Li, *Sep. Purif. Technol.*, 2025, **358**, 130292.

187 Z. Zhang, J. Liu, P.-Y. Gu, R. Ji, L. Jin, S. Zhou, J. He, D. Chen, Q. Xu and J. Lu, *Sep. Purif. Technol.*, 2022, **287**, 120539.